CHALMERS
UNIVERSITY OF TECHNOLOGY

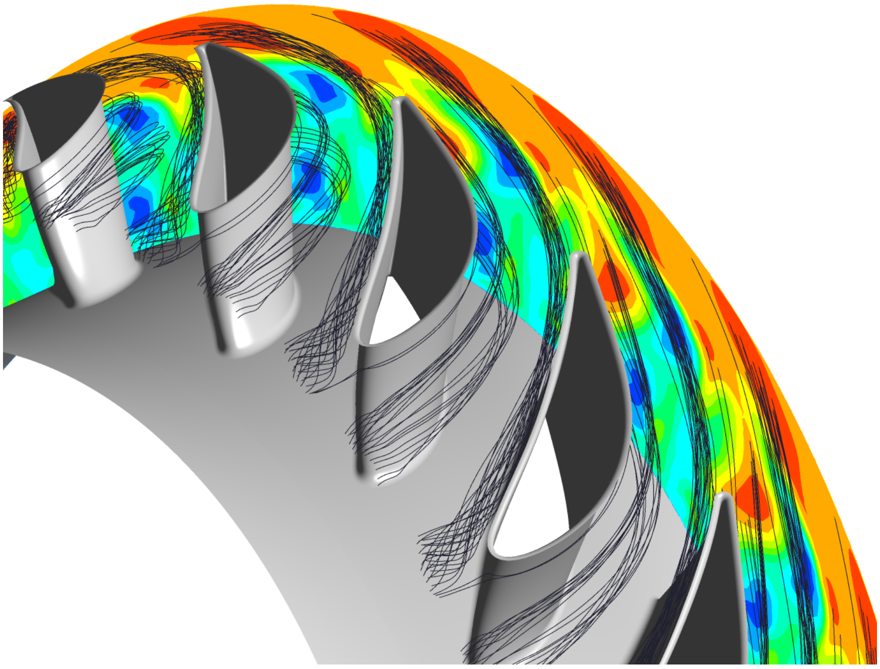

Unsteady 3D CFD analysis of a film-cooled 1½ stage turbine

Master's thesis in Applied Mechanics

JETHRO RAYMOND NAGAWKAR

Department of Applied Mechanics
CHALMERS UNIVERSITY OF TECHNOLOGY
Gothenburg, Sweden 2016

MASTER'S THESIS 2016:36

Unsteady 3D CFD analysis of a film-cooled 1½ stage turbine

JETHRO RAYMOND NAGAWKAR

CHALMERS
UNIVERSITY OF TECHNOLOGY

Department of Applied Mechanics
Division of Fluid Dynamics
CHALMERS UNIVERSITY OF TECHNOLOGY
Gothenburg, Sweden 2016

Unsteady 3D CFD analysis of a film-cooled 1½ stage turbine
JETHRO RAYMOND NAGAWKAR

© JETHRO RAYMOND NAGAWKAR, 2016.

Supervisor: Fredrik Wallin, GKN Aerospace and Carlos Arroyo, GKN Aerospace
Examiner: Niklas Andersson, Applied Mechanics

Master's Thesis 2016:36
Department of Applied Mechanics
Division of Fluid Dynamics
Chalmers University of Technology
SE-412 96 Gothenburg
Telephone +46 31 772 1000

Cover: IPV blade and hub along with streamlines of the tip leakage vortex of the rotor blades and total temperatures near the IPV trailing edge.

Gothenburg, Sweden 2016

Unsteady 3D CFD analysis of film-cooled 1½ stage turbine
JETHRO RAYMOND NAGAWKAR
Department of Applied Mechanics
Chalmers University of Technology

Abstract

Rising fuel costs and increasing global warming related issues have pushed jet engine manufacturers to increase the efficiency of their engines. One way of doing this is to increase the turbine inlet temperatures. This increases the specific work output of the turbine for a constant pressure drop across it, increasing its thermal efficiency. All the components located downstream of the turbine inlet are however subjected to increased material fatigue due to such high temperatures. This reduces the component life significantly and can also lead to severe engine damage. To reduce the effective surface temperatures, these parts need to be cooled both internally and externally.

In this thesis, how film cooling on the nozzle guide vanes (NGVs) of a 1½ stage turbine affects the downstream intermediate pressure (IP) vane has been studied. Point sources available in CFX have been used to model the flow through the cooling holes of the NGVs. The main focus is not to study film cooling on the NGVs, but to study how it affects the IP vane. The function of this vane is to guide the flow from the exit of the high pressure turbine to the IP rotor for further power extraction. The flow in the IP vane is extremely complex. It is affected heavily by the upstream non-uniformities such as tip leakage flows, cold streaks of the coolant, wakes from the blades as well as swirl and hot streaks from the combustion chamber.

Four different modeling approaches were studied; no film cooling steady and unsteady as well as film cooled steady and unsteady. The aerodynamic and heat transfer results from these simulations are compared to look for differences arising due to film cooling as well as unsteadiness in the flow to suggest guidelines for IP vane heat transfer analysis. The aerodynamic data is verified with experimental work done at the Oxford Turbine Research Facility (OTRF) by comparing the pressures at three different spans of the IP vane. The pressures at different hub and casing stations in the turbine have also been validated with these experiments.

Keywords: Turbine inlet temperature, CFX, NGV, IP, Aerodynamic, Heat transfer, OTRF, Pressure, Film cooling.

Contents

Abstract v

Preface ix

Nomenclature xi

List of Figures xv

List of Tables xvii

1 Introduction 1
- 1.1 Background 1
- 1.2 Aim 3
- 1.3 Scope and Limitations 3

2 Theory 5
- 2.1 Turbine basics 5
  - 2.1.1 3D flow 5
  - 2.1.2 3D flow features 6
  - 2.1.3 Turbine losses 7
- 2.2 Film cooling 7
  - 2.2.1 Parameters 8
    - 2.2.1.1 Downstream distance (x/D) 9
    - 2.2.1.2 Blowing ratio (M) 10
    - 2.2.1.3 Turbulence (Tu) 10
    - 2.2.1.4 Hole spacing (P/D) 10
    - 2.2.1.5 Inclination angle (α) 11
    - 2.2.1.6 Cooling hole length (L/D) 11
    - 2.2.1.7 Density ratio (ρ_c/ρ_∞) 12
  - 2.2.2 Coolant structure in cooling hole. 12
  - 2.2.3 How film cooling affects secondary flows. 12

3 Methods 15
- 3.1 Basic procedure 15
- 3.2 Flat plate analysis 15
  - 3.2.1 Cooling holes 15
  - 3.2.2 Source term simulations 16

3.2.3 Calculation of source term parameters 17
3.2.4 Resolved simulations 19
3.3 Turbine 20
3.3.1 Geometry 20
3.3.2 Mesh 20
3.3.3 Steady state simulations 21
3.3.4 Unsteady simulations 22
3.3.5 Set-up and boundary conditions 22
3.3.6 Point source and cell face source methods. 22
3.3.7 Fully turbulent model v/s transitional model. 23

4 Results and Discussions 25
4.1 Flat plate simulations 25
4.1.1 Hole 1: Resolved v/s source term cooling hole simulations . . 25
4.1.2 Hole 2: Resolved v/s source term cooling hole simulations . . 28
4.2 Turbine simulations. 31
4.2.1 Pressures and temperatures on the IPV surface. 31
4.2.2 Rotor inlet 32
4.2.3 Flow features in the rotor 34
4.2.4 IPV inlet in the relative frame of reference. 34
4.2.5 Vortex formation in the rotor domain 36
4.2.6 IPV inlet in the stationary frame of reference. 37
4.2.7 Flow in the IPV domain. 37
4.2.8 CFD v/s experimental data. 40
4.2.8.1 Pressure on IPV surface. 40
4.2.8.2 Hub and casing pressures at different stations in the turbine. 42

5 Conclusion 45
5.1 Flat plate simulations. 45
5.2 Turbine simulations. 45
5.2.1 Aero 45
5.2.2 Heat transfer. 45
5.3 Future work. 46

Bibliography 47

A Transitional model. I

Preface

This thesis is part of a larger collaboration between Oxford University, Rolls Royce plc. and GKN Aerospace within the EU FP7 project LEMCOTEC. It was carried out at GKN Aerospace Trollhättan. I would like to thank Paul Beard at Oxford University for providing me the experimental data required for validating my results. I am also grateful to Mark Stokes at Rolls Royce for providing the rotor mesh. In addition, I like to express my gratitude towards Lars Ljungkrona at GKN Aerospace for helping out with the meshing of the turbine as well as giving me software related support. I would like to thank my examiner Niklas Andersson for his administrative related support. Finally, I would like to thank my advisers Fredrik Wallin and Carlos Arroyo at GKN Aerospace for providing me all the help and support required to carry out this master thesis.

Jethro Raymond Nagawkar, Gothenburg, June 2016

Nomenclature

Latin Symbols

C	chord length
D	cooling hole diameter
k	turbulent kinetic energy
l	turbulent length scale
L	cooling hole length
M	blowing ratio
$\hat{n}$	directional vector of cooling hole
N	cell face length
P	hole spacing and pressure (static)
P_0	total pressure
Re	Reynolds number
T	temperature
T_0	total temperature
T_u	turbulence intensity
U	coolant velocity
x	streamwise distance
X	axial direction
Y	circumferential direction
Z	radial direction
x, y, z	cartesian coordinates
y^+	dimensionless wall distance

Greek Symbols

α	inclination angle
ρ	density
ω	specific dissipation rate

Subscripts

0	cooling hole inlet
1	cooling hole outlet
in	inlet
c	coolant
x	streamwise direction
y	circumferential direction
z	spanwise direction
∞	free stream

Abbreviation

2D	two-dimensional
3D	three-dimensional
CAD	computer aided design
CFD	computational fluid dynamics
IP	intermediate pressure
IPV	intermediate pressure vane
HPT	high pressure turbuine
MRF	multiple reference frames
NGV	nozzle guide vane
SST	shear stress transport
OTRF	Oxford turbine research facility

List of Figures

1.1 Trend of turbine inlet temperatures with year [2]. 1
1.2 Film cooled turbine blade [3]. 2
1.3 Meridional view of the turbine. 2
1.4 NGV with the selected cooling holes for flat plate simulations. 4

2.1 2D flows [3]. 5
2.2 Secondary flows in a turbine blade passage [3]. 6
2.3 Tip leakage flow [3]. 7
2.4 Film cooled turbine blade along with the cooling holes [4] [3]. 8
2.5 Cut-section of a turbine blade showing the cooling hole angles [4]. . . 9
2.6 Downstream distance. 9
2.7 Spacing between 2 cooling holes. 10
2.8 Inclination angles. 11
2.9 Cooling hole length. 11
2.10 The coolant structure on exiting the cooling hole [12]. 12

3.1 Cooling hole angles. 16
3.2 Mesh resolutions for the point source method. 17
3.3 Resolved simulation mesh for hole 1. 19
3.4 NGV. 20
3.5 NGV mesh for film cooled simulations. 21
3.6 Meridional view of the turbine showing the stationary (yellow), cavities (green) and rotating (orange) parts of the rotor domain hub. . . . 23

4.1 $T_0/T_{0,in}$ and Mach Number contours in a meridional cut-plane ($0 <$ x/D < 65). 26
4.2 $T/T_{0,in}$ contours on the plate ($0 <$ x/D < 65). 26
4.3 $T_0/T_{0,in}$ contours at cut-planes x/D = 0, 5, 10, 15. 27
4.4 $T_0/T_{0,in}$ at the outlet. 28
4.5 $T_0/T_{0,in}$ and Mach Number contours in a meridional cut-plane ($0 <$ x/D < 60). 29
4.6 $T/T_{0,in}$ contours on the plate ($0 <$ x/D < 60). 29
4.7 $T_0/T_{0,in}$ contours at x/D = 0, 5, 10, 15. 30
4.8 $T_0/T_{0,in}$ contours at the outlet. 30
4.9 $P/P_{0,in}$ on the IPV surface. 31
4.10 $T/T_{0,in}$ on the IPV surface. 32
4.11 $P_0/P_{0,in}$ and $T_0/T_{0,in}$ at rotor inlet. 33

4.12 Streamlines showing vortex formation. 34
4.13 Time averaged $T_0/T_{0,in}$ at IPV inlet in the relative frame of reference. 35
4.14 Time averaged $P_0/P_{0,in}$ at IPV inlet in the relative frame of reference. 35
4.15 $P_0/P_{0,in}$ contours showing regions of losses. 36
4.16 Time averaged IPV inlet $P_0/P_{0,in}$ and $T_0/T_{0,in}$. 37
4.17 Time averaged $P_0/P_{0,in}$ at different cut-section in the IPV domain . . 38
4.18 Time averaged $P_0/P_{0,in}$ at 30% span in the IPV domain 38
4.19 Time averaged $T_0/T_{0,in}$ at different cut-section in the IPV domain (film cooled). 39
4.20 Time averaged $T_0/T_{0,in}$ at 50% span in the IPV domain (film cooled). 39
4.21 Time averaged IPV hub $T/T_{0,in}$. 39
4.22 Time averaged IPV casing $T/T_{0,in}$. 40
4.23 Pressures on IPV surface at 10% span. 40
4.24 Pressures on IPV surface at 50% span. 41
4.25 Pressures on IPV surface at 90% span. 42
4.26 Location of pressure measurements. 42

A.1 Wall shear stress. I

List of Tables

3.1 Cell face sizes used in point source term model. 16
3.2 Source term quantities. 19
3.3 Number of cells in each domain of the turbine along with y^+ and the meshing tool used to generate the mesh. 21

4.1 Hub and casing static pressures. 43
4.2 Percentage errors in hub and casing static pressures. 43

1

Introduction

This chapter will give a basic overview of the thesis. It will also discuss the aims, scopes and limitations of the thesis.

1.1 Background

In modern aero engines, the temperatures in-between the combustor exit and inlet to the high pressure turbine (HPT) have already exceeded 2000°C [1]. The trend by engine manufacturers is to increase this temperatures even further, as shown in Figure 1.1. This increase improves the efficiency of the turbine, reducing the amount of fuel consumed which in turn saves the airline industry millions of dollars.

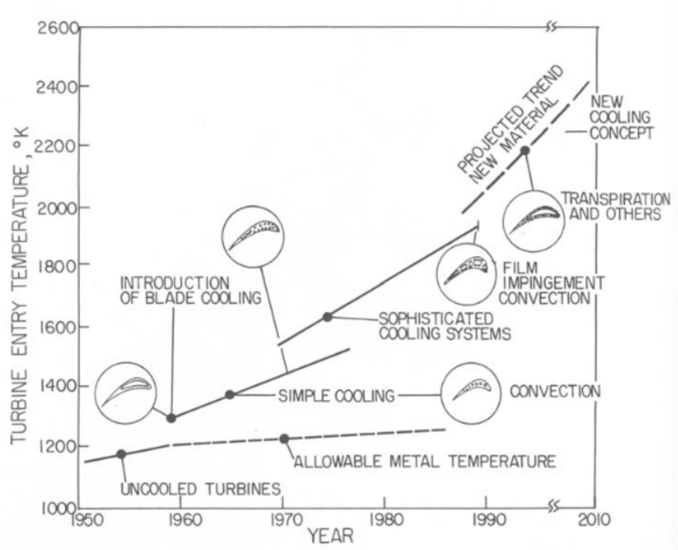

Figure 1.1: Trend of turbine inlet temperatures with year [2].

Increasing turbines inlet temperatures also has a downside. All the components located downstream of the combustor are subjected to higher thermal loads due to such high temperatures. This increases the material fatigue of the components, which can lead to cracks and could possibly cause severe engine damage. To reduce the effective surface temperatures, the components need to be cooled both internally and externally.

In this thesis, the interest is in external cooling, namely, film cooling of the nozzle guide vanes (NGVs) of a HPT. Film cooling, as the name suggests, is basically a layer of cold fluid on the surface of the component. This fluid is generally extracted from the exit of the compressor system and fed to the interior of the HPT. The fluid then flows onto the surface of the HPT via the cooling holes. This then creates a layer of thin cold fluid on the surface of the HPT. The cooling arrangement on a turbine blade can be seen in Figure 1.2.

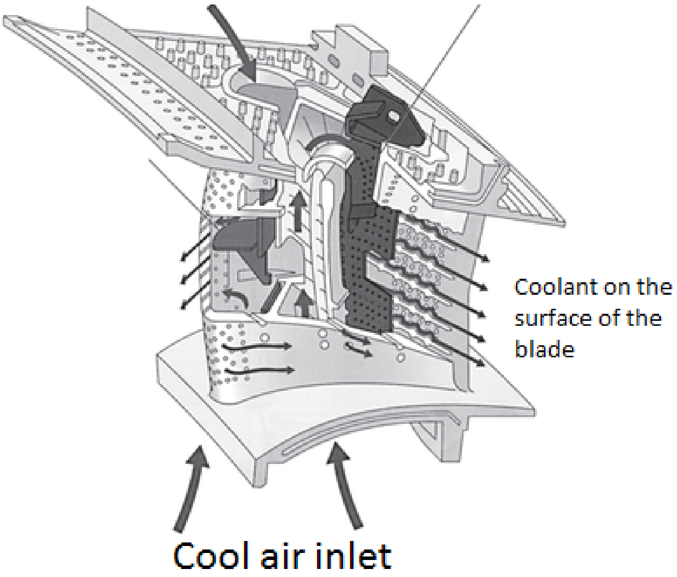

Figure 1.2: Film cooled turbine blade [3].

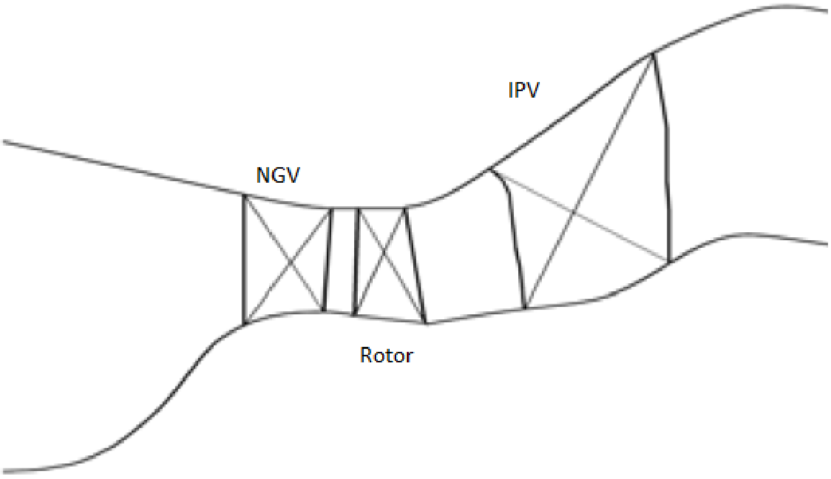

Figure 1.3: Meridional view of the turbine.

In this thesis, how film cooling on the NGVs of a 1½ stage turbine affects the downstream intermediate pressure vane (IPV), is studied. The turbine we study is a one stage HPT followed by the IPV. It has 40 NGVs, 60 rotor blades and 20 IPVs. The simulation domain however, consists of 2 NGVs, 3 rotor blades and 1 IPV with a rotational periodicity boundary condition. This boundary condition models the flow through the entire 360°of each blade row. A meridional view of the turbine is shown in Figure 1.3. The focus of this thesis is not on the film cooling of the NGVs, but on how this film cooling affects the flow and heat transfer in the IPV. The function of this vane is to guide the flow from the exit of the HPT to the intermediate pressure rotor for further power extraction. The flow in the IPV is extremely complex. It is affected heavily by the upstream non-uniformities such as tip leakage flows, cold streaks of the coolant, wakes from the blades as well as due to the swirl and temperature non-uniformities from the combustor.

1.2 Aim

The aim of this thesis is to study how film cooling on the NGVs affect the aero and heat transfer properties of the flow on the downstream IPV. This thesis is not aimed at studying film cooling on the NGVs. It will involve developing a method of implementing film cooling in ANSYS CFX. This method needs to be quick and easy to implement. It should also be applicable for other turbine designs. The CFD results will also be validated using experimental results obtained in the Oxford Turbine Research Facility.

1.3 Scope and Limitations

The main focus of this thesis is how the IPV is affected by film cooling on the NGVs. Film cooling effects on the NGVs themselves is not studied. Point sources in ANSYS CFX were used to setup the film cooling model. This model specifies the coolant temperatures, mass flow rates, direction of coolant ejection, turbulent kinetic energy (k) and specific dissipation rate (ω) for each cooling hole. This method specifies these quantities to the cell face closest to the locations specified by the user. In this case, the locations are the cooling hole exits on the surface of the NGVs

The point source method is highly mesh dependent. It specifies the mass and energy source terms. However, the momentum source term is controlled by the cell face area. For a given mass flow rate, a change in cell face size, affects the velocity of the coolant.

To find this cell size, 2 different cooling holes on the NGV were investigated (Figure 1.4). The holes had different inclination angles as well as mass flow rates. For the first cooling hole, the point source term method was implemented for different cell face sizes and compared to a fully resolved cooling hole simulation. The optimum cell face size setting found was then compared with a fully resolved simulation for the second cooling hole.

The point source method does not always specify the source terms on the cell faces the user specifies. In this study, it would specify the source terms on cell faces in the boundary layer for some locations. The final simulations of the turbine done, has specified source terms by picking individual cell faces. This method specifies the exact same quantities as the point source term method. The results obtained for the flat plate were exactly the same. This method is however, more time consuming as it requires the user to pick individual cell faces.

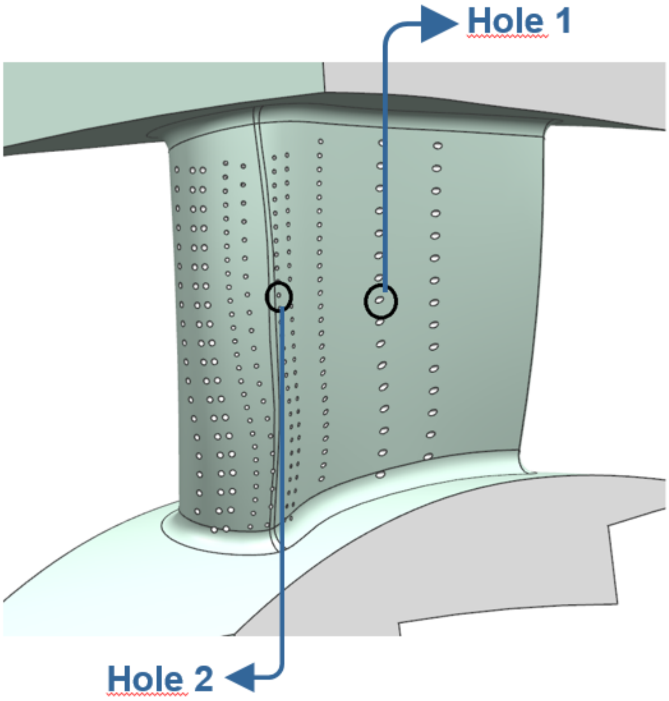

Figure 1.4: NGV with the selected cooling holes for flat plate simulations.

The data provided for the simulations, specifies the mass flow rate for each cooling row. This has been divided equally per cooling hole. However, in reality, the mass flow rate through each hole is expected to vary both in the spanwise and streamwise direction.

The flow exiting the cooling hole is extremely complex. To capture its structure near the NGV surface, more complex correlations need to be developed. Numerous studies have already been done and can be found in [8], [14], [15] and [9] etc. However, none of these have been implemented as part of this thesis.

Initial steady and unsteady simulations without film cooling were done to study the flow in the turbine. These 2 simulations have a lower total inlet temperature. This temperature was calculated by doing a mass flow average of the actual inlet total temperatures and coolant total temperatures. These 2 simulations were used as a baseline and compared to the film cooled steady and unsteady simulations. This way, differences in results arising due to film cooling and/or by unsteadiness in the flow can be seen.

2

Theory

2.1 Turbine basics

2.1.1 3D flow

Far enough from the endwalls, the radial component of velocity in blades with high hub to tip ratios can be neglected and the flow can be approximated as 2D. However, when the hub to tip ratio falls below 0.8[3], the radial velocity distribution becomes appreciable. This leads to redistribution of the mass flow, which in turn affects the outlet velocity profile. A radial velocity is caused by a temporary imbalance between the centrifugal force acting on a fluid and the radial pressure within the fluid. A radial equilibrium method is commonly used in design calculation of turbines and compressors. This method assumes that radial flow occurs within a blade passage, the flow outside the row being in radial equilibrium. It also assumes that that the flow is axisymmetric, implying that the effects of the discrete blades are not transmitted through the flow. 3D flows can be represented as a combination of a pair of 2D flows namely the blade to blade and the meridional streamsurface flows (Figure 2.1a). These 2 methods are of limited accuracy, but remain a key feature in turbomachinery design. Cascade analysis (Figure 2.1b) and blade to blade computational methods are used to determine blade to blade flows while radial equilibrium and through flow methods are used to study meridional flows. 3D flows in gas turbines are extremely complex and can now be modelled using CFD.

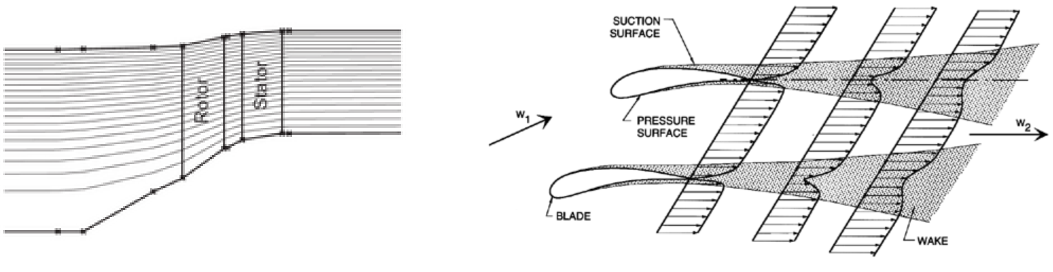

(a) Through flow computation.

(b) Cascade analysis.

Figure 2.1: 2D flows [3].

2.1.2 3D flow features

The flow in a turbomachine is extremely complex and varies in the axial, radial and tangential directions. Designing the blades in a turbomachine using blade to blade and meridional streamsurface calculation methods is not sufficient as they cannot capture the finer 3D details in the flow. These features can affect the performance of a turbomachine quite significantly. Some of these features are discussed below.

Secondary flow

Vorticity is present in boundary layers of the end wall. When the flow is turned through the blade rows, the vorticity vector is turned as well, generating secondary vorticity parallel to the outlet stream direction. This flow feature cannot be captured by 2D models. This is further complicated as the vorticity is split at the leading edge of the blades. The vortex at the pressure side of the blade is swept to the suction side of the adjacent blade, forming the passage vortex. The vortex at the suction side sticks to this side and interacts with pressure side vortex closer to the trailing edge. This leads to complex flow structures as well as increased mixing and shear related losses.

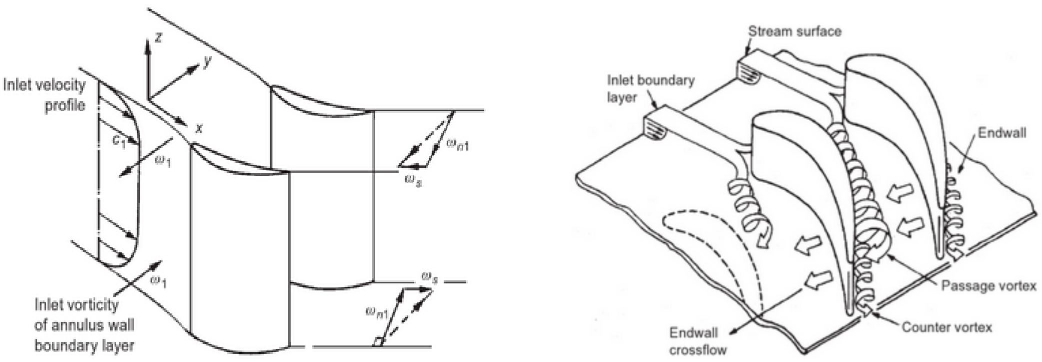

Figure 2.2: Secondary flows in a turbine blade passage [3].

Tip gap flow

The rotor blades in compressors and turbines have a gap between the blade tips and the outer casing which creates a flow path for the fluid as shown in Figure 2.3. Gas flows from the pressure side of the blade to the suction side nearly perpendicular to the main flow path. The fluid generally separates at the pressure side corner in the tip gap, creating a separation bubble, contracting the available flow area. The flow then emerges as a high velocity jet at the suction side. Shear is developed between the tip gap flow and the main flow, generating a vortex with a rotational axis aligned with the main flow in the blade passage. Significant losses are developed due to shear in the tip gap as well as shear and mixing between the tip gap flow and the main flow. These losses account for nearly one third or more of the total losses in a turbomachine [5].

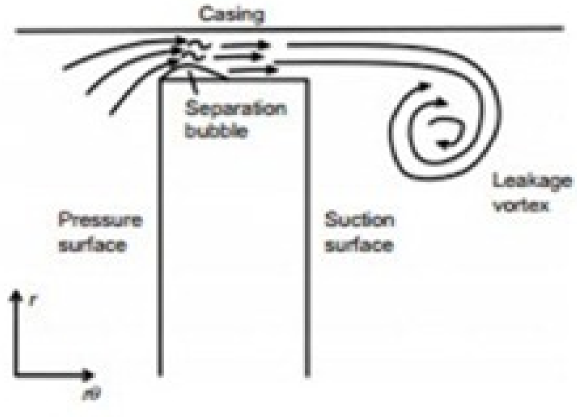

Figure 2.3: Tip leakage flow [3].

2.1.3 Turbine losses

There are numerous sources of loss in turbines. A detailed description of the different types of loss mechanisms is given in Denton[5]. Losses in fluid flows result in entropy generation. This entropy generation is caused by various irreversible processes like viscous friction, shock waves, heat transfer across a finite temperature difference and mixing between fluids of different properties. Losses in turbines are categorized as 2D losses; these include boundary layer losses, trailing edge mixing, flow separation and losses due to shock waves and 3D losses: these include tip leakage flows, endwall flows and coolant flows. These losses can affect the distribution of pressure and temperatures on downstream components.

2.2 Film cooling

Rising fuel cost, increasing emissions and increasing global warming related problems have pushed aircraft engine manufacturers to increase the efficiency of the gas turbine. One way of doing this is by increasing the turbine inlet temperature. Increasing the turbine inlet temperature, increases the specific work output of a turbine for a constant pressure drop across the turbine. This increases the thermal efficiency of the gas turbine[7]. Increasing the turbine inlet temperature increases the specific thrust while reducing the specific fuel consumption[3] as well.

Today's gas turbines reach temperatures in excess of 2000°C [1] at the exit of the combustor and inlet of the high pressure turbine. At such high temperatures, even turbine blades made of nickel-based alloys will melt .Higher temperatures are also responsible for increased material fatigue of the downstream components. This leads to reduced component life and also increases the possibility of cracks. The engine can also be severely damaged. To reduce the effective component surface temperatures, both external and internal cooling is required for the turbine. Cooler air at around 700°C from the exit of the compression system is fed directly to the interior of the high pressure turbine blades. Cooling holes are present to allow the air to travel to the exterior of the blades, forming a cooling film on the surface of the blades. This cooling film reduces the surface temperature of the blades. Figure 2.4, shows the internal and external flow of the coolant for a turbine blade along with the cooling holes.

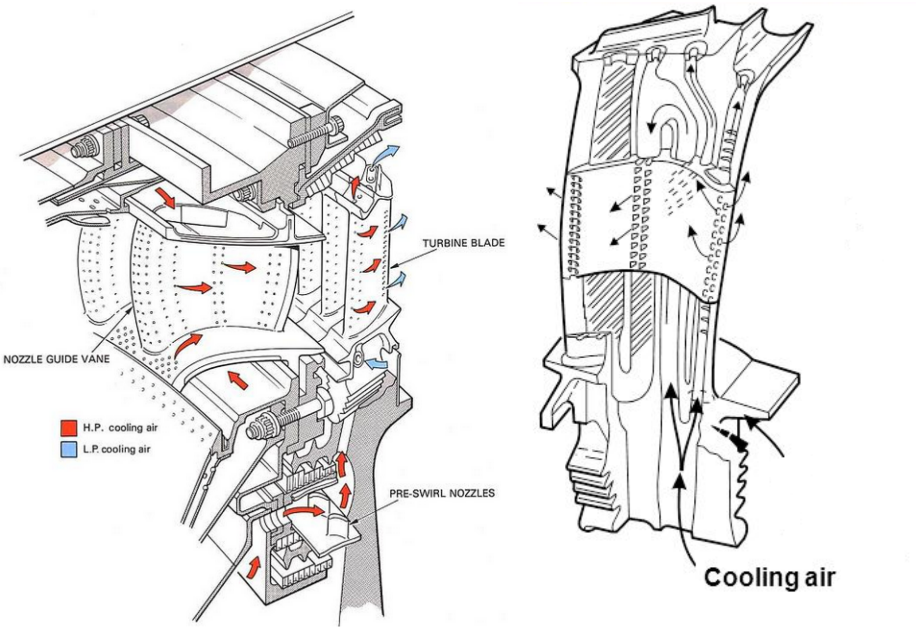

Figure 2.4: Film cooled turbine blade along with the cooling holes [4] [3].

There are two different types of film cooling; transpiration cooling and effusion cooling. Transpiration cooling is the most efficient type of cooling present as it allows for an even amount of coolant per unit area. It is basically similar to a wall with infinite number of holes, like the pores in our skin. However, there is no such material that has an infinite number of holes and that can fulfil the design requirement of the turbine blades. For this reason, effusion cooling is used. It is basically cooling through holes. These holes are laser drilled and have diameters around 1mm. The angle at which they are drilled, generally lies between 15 and 45 degrees[6]. Figure 2.5, shows the cut-section of a turbine blade showing the cooling hole angles.

Coolant flow is extracted from the exit of the compressor system and accounts for about 5% of the core mass flow. It bypasses the combustor and reduces the amount of air used in the combustion process. Therefore less energy is transferred to the turbine. External cooling flows are also responsible for unwanted secondary flows, which reduces the efficiency of the engine. Too much coolant decreases the efficiency of the engine and too little coolant will result in heat overload. This heat overload will result in reduced component life and can lead to severe engine damage. It is therefore essential to have the coolant distributed properly over the blades and in correct amounts.

2.2.1 Parameters

The following subsection discusses some important parameters that affect film cooling. These parameters play an important role in developing correlations to capture

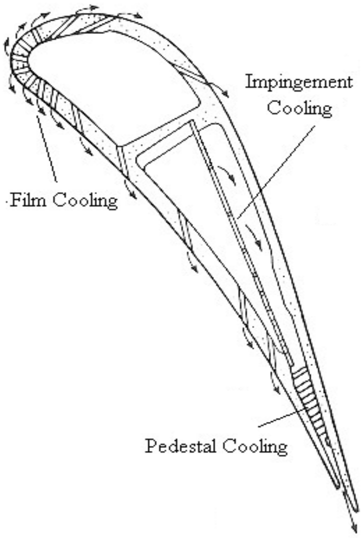

Figure 2.5: Cut-section of a turbine blade showing the cooling hole angles [4].

the structure and flow properties of the coolant at the exit of the cooling hole[8]. It must be noted that several individual author, e.g. [8] and [9], neglect few of the parameters while developing their correlations. This results in different mathematical models for the source terms. A study done by Kampe and Völker [10] has shown that even the least significant parameter can play a major role in predicting film cooling effectiveness.

2.2.1.1 Downstream distance (x/D)

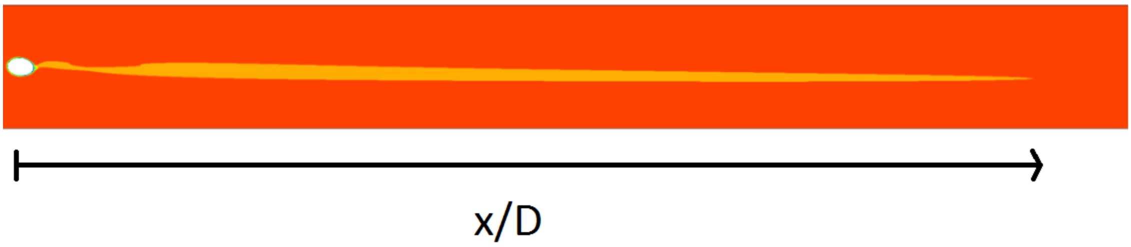

Figure 2.6: Downstream distance.

Film cooling effectiveness is commonly plotted as a function of downstream distance. Figure 2.6, shows the surface of a flat plate with the downstream distance. It is normalized with hole diameter to compare different cooling hole sizes. Depending on whether the coolant separates at the cooling hole exit, the location of the maximum film cooling effectiveness varies. If there is no separation, the maximum effectiveness is downstream and adjacent to the hole exit. In the case of separation, it moves further downstream. The coolant in this case, mixes with the free stream and is brought back to the blade surface. An optimum amount of separation will distribute the coolant more evenly while keeping its temperature low enough for an effective cooling.

2.2.1.2 Blowing ratio (M)

Blowing ratio is defined as the ratio of coolant density (ρ_c) times the coolant velocity (U_c) divided by the free stream density (ρ_∞) times the free stream velocity (U_∞).

$$M = \frac{\rho_c U_c}{\rho_\infty U_\infty}$$

At lower blowing ratios, the coolant does not separate at the cooling hole exit. This leads to a peak film effectiveness at the hole exit. At higher blowing ratios, the peak film effectiveness is moved further downstream as the flow separates.

Work done by Baldauf et. al[11] on film effectiveness for rows of cylindrical holes showed exactly this. For low blowing ratios, they found peak effectiveness at the hole exit, while the overall effectiveness was extremely low. This is due to low mixing with the free stream and hence insufficient spreading of coolant on the blade surface. On further increasing the blowing ratio, both the peak and overall film effectiveness increased with the peak effectiveness moving downstream. At one point defined as "moderate blowing ratios" by Baldauf et. al, the peak effectiveness decreased while the overall effectiveness continued to increase. This was attributed to hot air entrapment between the jet and the surface leading to more mixing between the coolant and the free stream. A maximum overall effectiveness was found at M=1. At higher blowing ratios, the jet penetrates too deep into the main flow to have any effect on the surface.

2.2.1.3 Turbulence (Tu)

Saumweber and Schulz[13] studied the effect of increased free stream turbulence on film cooling effectiveness. They found that when the free stream turbulence was increased for low blowing ratios, the film cooling effectiveness dropped near the hole exit as more mixing took place between the free stream and the coolant, leading to higher temperatures on the surface. For higher blowing ratios, when the free stream turbulence was increased, the mixing led to the coolant being transported quicker to the surface leading to higher film cooling effectiveness. Increased turbulence also increased jet interaction between adjacent cooling holes, leading to a further increase in film cooling effectiveness.

2.2.1.4 Hole spacing (P/D)

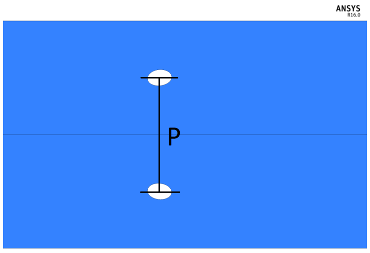

Figure 2.7: Spacing between 2 cooling holes.

For a given blowing ratio, smaller the hole spacing (Figure 2.7), the more coolant mass flow rate per area. This leads to increased film cooling effectiveness as investigated by Bauldauf et. al.[11]. Jet interaction is increased as well. For a hole spacing of P/D greater than 5, Bauldauf et. al. found no adjacent jet interaction for x/D less than 80.

2.2.1.5 Inclination angle (α)

Inclination angle affects how the coolant is distributed in the normal and tangential direction. At low inclination angles, the coolant does not separate from the surface as easily, while at higher inclination angles it does, leading to more jet penetration. Similar to higher blowing ratios, the increased jet penetration increases mixing, leading to more surface coverage. But unlike high blowing ratios, the enhanced coverage does not compensate for the lack of film cooling in the separated region[14]. Low inclination angles are preferred, but these are generally difficult to manufacture. Figures 2.8a and 2.8b show high and low inclination angles respectively.

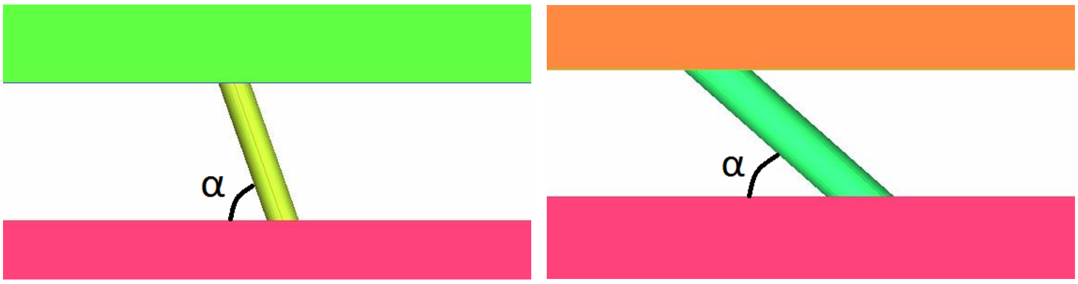

(a) High.

(b) Low.

Figure 2.8: Inclination angles.

2.2.1.6 Cooling hole length (L/D)

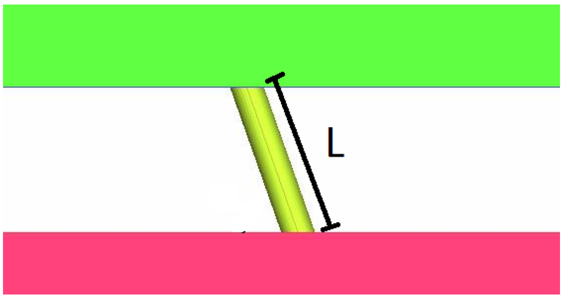

Figure 2.9: Cooling hole length.

The cooling hole length (Figure 2.9) impacts the film cooling effectiveness significantly. For short hole lengths, turbulence caused due to flow separation at the inlet, does not get dissipated before exiting the cooling hole. This leads to flow separation at the hole exit and higher jet penetration, which enhances the mixing with the main flow[14]. This leads to better coverage over the surface but with a poor overall film cooling effectiveness compared to longer cooling hole lengths.

2.2.1.7 Density ratio (ρ_c/ρ_∞)

The ratio of the density of the coolant to the density of the free stream is called the density ratio. The study done by Bauldauf et. al.[11] found that the peak effectiveness was reduced for lower density ratios and so did the blowing ratio at which the peak effectiveness was reached. The two blowing ratios chosen for the study reached the same overall effectiveness. The density ratio of 1.2 with a blowing ratio of 0.7, reached the same overall effectiveness as the density ratio of 1.8 with a blowing ratio of 1.0. This means that at lower mass flows, the same overall effectiveness can be reached if lower densities of coolant is used.

2.2.2 Coolant structure in cooling hole.

The coolant structure in the cooling hole is 3D. On entering the cooling hole, the coolant separates. This contracts the area available for the coolant to flow, creating a jetting effect. This leads to increased velocities and forms a counter rotating vortex pair. Upon exit, the coolant modifies the local pressure. The pressure upstream of the hole is increased, whereas the pressure downstream is decreased. This bends the coolant onto the surface. The flow accelerates above and around the coolant and decelerates upstream and downstream of it. The deceleration of the flow upstream leads to separation of the boundary layer and a horseshoe vortex that wraps around the coolant. The coolant structure on exiting the cooling hole is shown in Figure 2.10.

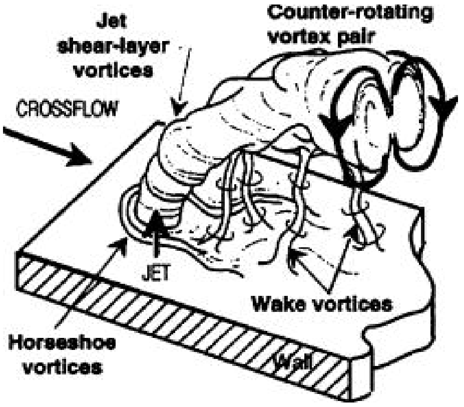

Figure 2.10: The coolant structure on exiting the cooling hole [12].

2.2.3 How film cooling affects secondary flows.

A basic study on the influence of film cooling on the secondary flow in a turbine nozzle was done by Langowsky and Vogel[16]. They performed both an experimental and a CFD study for a single row of cooling holes present close to the trailing edge of the NGVs. They conducted this study for three different blowing ratios; 0, 0.5 and 1.4. For a blowing ratio of 0.5, the secondary flow deflected the coolant, due to its low momentum. For the higher blowing ratio of 1.4, the coolant deflects the secondary flow to a nearly axial-directed propagation, pushing the passage vortex to the end walls. This reduces the region of influence of the secondary flow, resulting in a more uniform outlet.

3

Methods

3.1 Basic procedure

The work done can be broken down into 3 major parts. The first part involves performing both steady and unsteady simulations of the turbine, without film cooling. The inlet total temperature for these simulations is obtained by doing a mass flow average of the coolant total temperature and the total temperature of the inlet flow. These simulations were done in order to get a first analysis and for the later comparison with the simulations which include cooling. In this way, the effect of film cooling on the downstream components as well as effects due to unsteadiness were analyzed. In the second part, two different cooling holes were selected and a flat plate simulations were done comparing a point source term model to a fully resolved cooling hole simulation. The aim is to find the correct cell face lengths in the span and streamwise directions on the plate surface. Point sources were used to specify the total mass flow rates and temperatures in a cell face closest to the specified location. In order to get the correct momentum flux, the correct cell face size needs to be found. Different cell face sizes in the point source term model were evaluated. The selected cell face size is then rechecked with the second cooling hole. This cell face size is then used as the size of the cells on the surface of the NGVs in the final film cooling simulation. The steady and unsteady film cooled turbine simulations is the third part.

3.2 Flat plate analysis

3.2.1 Cooling holes

The location of the two cooling holes on the blade surface is shown in Figure 1.4. The reason for choosing these two cooling holes is that they have different diameters, mass flow rates, angles with respect to the horizontal and vertical directions (Figure 3.1) and are located in different places on the blade. It must be noted that these two holes are rotated to make the tangent to the blade surface horizontal along the +X direction. The flat plate was made long enough, as the interest is in studying the flow downstream. In this case, it is the same length as the turbine (X axis). The height of the domain (Y axis) was set to about 5mm and the the width (Z direction) was set to the average distance between two holes in that row.

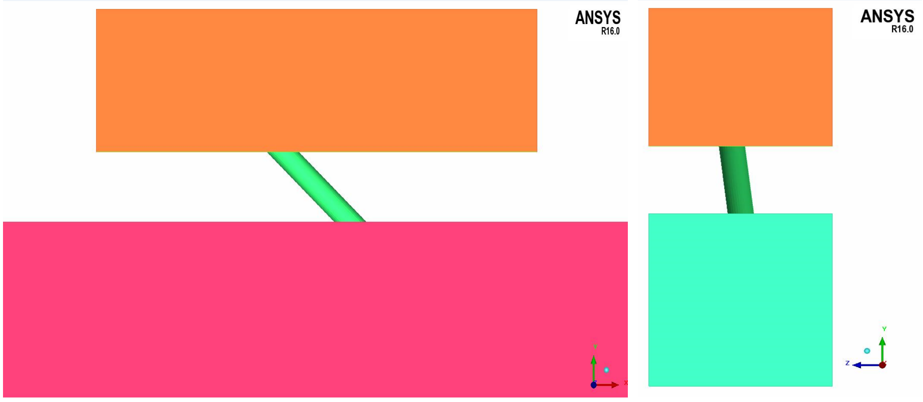

(a) Hole 1.

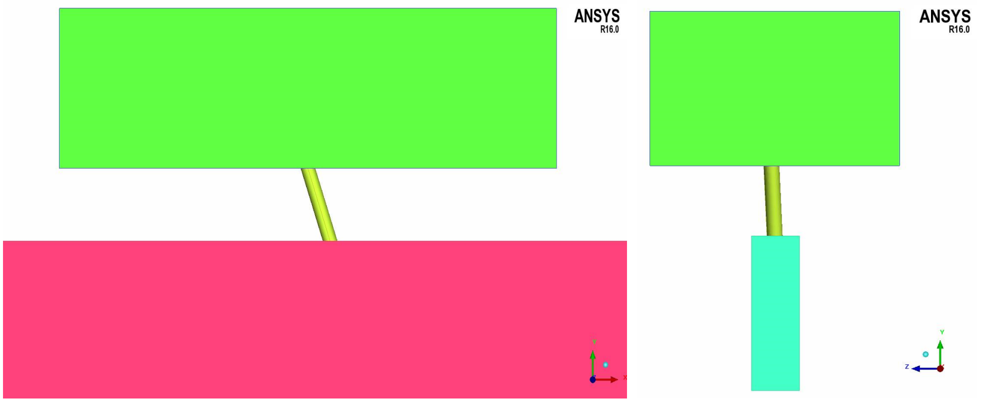

(b) Hole 2.

Figure 3.1: Cooling hole angles.

3.2.2 Source term simulations

For cooling hole 1, four different cases (Table 3.1) with varying cell face size in the spanwise and streamwise directions were used to compare the point source method with the resolved cooling simulation. Note that, case 2 and 3 have the same cell sizes, but the source term is equally distributed amongst 4 neighbouring cells, closest to the cooling hole exit. The case which showed the best results, was used to compare the resolved and the source term method for hole 2. This cell face size was then used as the mesh size on the surface of the NGV. Note that N_x and N_z are the cell face lengths in the X and Z directions.

Case	N_x/D	N_z/D	No. of source points	No. of cells
1	1	1	1	198,800
2	2	2	1	662,200
3	2	2	4	662,200
4	1.5	1.5	1	364,100

Table 3.1: Cell face sizes used in point source term model.

The mesh was created in ICEMCFD. A structured hexahedral mesh was created from a single block. The geometry being a cuboid, all the cells were near perfect cuboids with the quality being close to 1. The plate had a y^+ of around 1 and a growth ratio of 1.2 was used for the boundary layer mesh. The number of cells is listed in Table 3.1. The three different mesh sizes are shown in Figure 3.2.

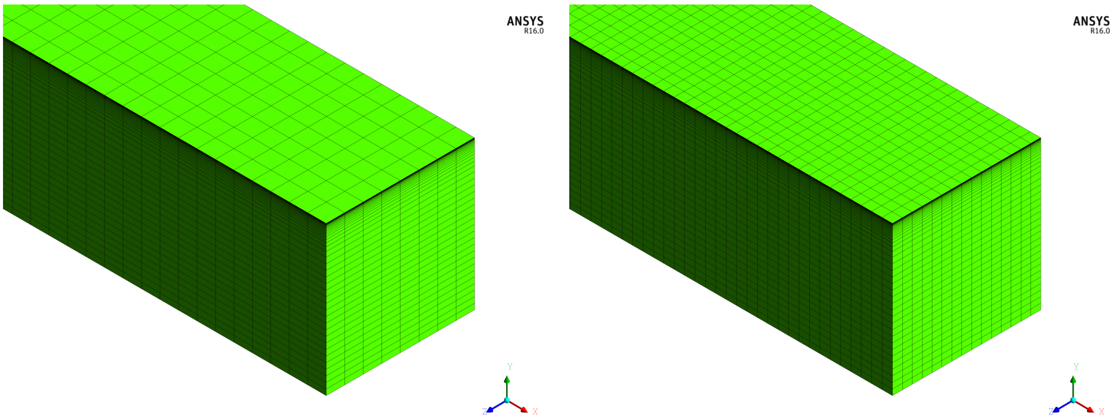

(a) Case 1.

(b) Case 2 and 3.

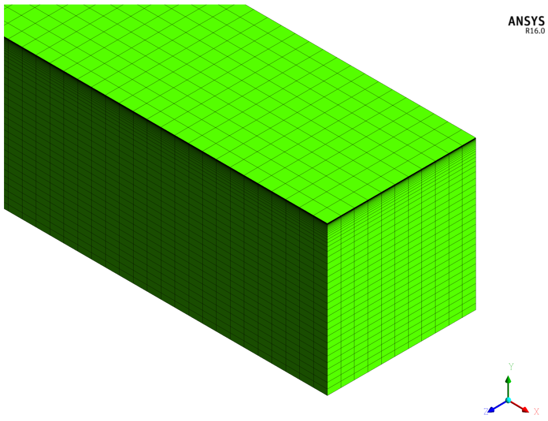

(c) Case 4.

Figure 3.2: Mesh resolutions for the point source method.

The same inlet boundary conditions as those of the film cooled turbine were used for the flat plate simulations. The outlet static pressure was set to 0.976 times the inlet total pressure. This pressure was obtained by matching the Mach number near the cooling hole from the turbine simulations, for hole 1. The flat plate was set to a no-slip wall, the boundary opposite to it was set to a free slip wall and the adjacent boundaries were set to a translational periodicity boundary condition. These same conditions were used for hole 2.

3.2.3 Calculation of source term parameters

This section demonstrates how the quantities in the point source method are calculated.

Location

The location of the hole inlet and exit is taken from the CAD geometry. The cooling hole exit is used to specify the location of the point source. It is given by cartesian coordinates (x_1, y_1, z_1).

Mass flow rate

The total mass flow rate was provided for each cooling row. This was divided by the number of holes in that row to get the mass flow rate through each individual hole. Note that the mass flow rate may vary radially across the blade. But in this thesis, it is assumed to be equal.

Temperature

The temperature was set to the coolant temperature. This temperature is about 0.61 times the inlet total temperature. Potential heating of the coolant inside the cooling hole was not included.

Turbulent kinetic energy (k)

Reynolds number

$$Re = \frac{\rho_c U_c D}{\mu_c}$$

Turbulent intensity

$$T_u = 0.16(Re)^{(-1/8)}$$

Turbulent length scale

$$l = 0.07D$$

$$k = \frac{3}{2}(U_c T_u)^2$$

Specific dissipation rate (ω)

$$\omega = (0.09)^{(-1/4)}\frac{k^{3/2}}{l}$$

Both k and ω are calculated by using equations of turbulent pipe flow.

Directional vector

This vector specifies the direction in which the coolant exits the cooling hole. It is a unit vector along the line joining the center of the cooling hole exit and inlet and facing the hole exit.
Coordinates of cooling hole inlet: (x_0, y_0, z_0)
Coordinates of cooling hole exit : (x_1, y_1, z_1)
Directional unit vector:

$$\hat{n} = \frac{(x_1 - x_0)\hat{\imath} + (y_1 - y_0)\hat{\jmath} + (z_1 - z_0)\hat{k}}{\sqrt{(x_1 - x_0)^2 + (y_1 - y_0)^2 + (z_1 - z_0)^2}}$$

Source term quantity
Mass flow rate (kgs^{-1})
Temperature (K)
k (m^2s^{-2})
ω (s^{-1})
U_x (ms^{-1})
U_y (ms^{-1})
U_z (ms^{-1})

Table 3.2: Source term quantities.

The source term quantities set are listed in table 3.2. Note that the velocity components, namely U_x, U_y, U_z are used by CFX to specify the direction of fluid ejection and not the velocity.

3.2.4 Resolved simulations

The meshes for the resolved simulations were created in ICEMCFD using the structured hexahedral blocking technique. The minimum cell qualities for hole 1 and 2 are 0.52 and 0.48 respectively. All wall type boundary conditions have a y^+ of around 1 with a growth ratio of 1.2. The total number of cells generated were 10.75 million for hole 1 and 13 million for hole 2. Figure 3.3 shows the mesh generated for the cooling hole 1.

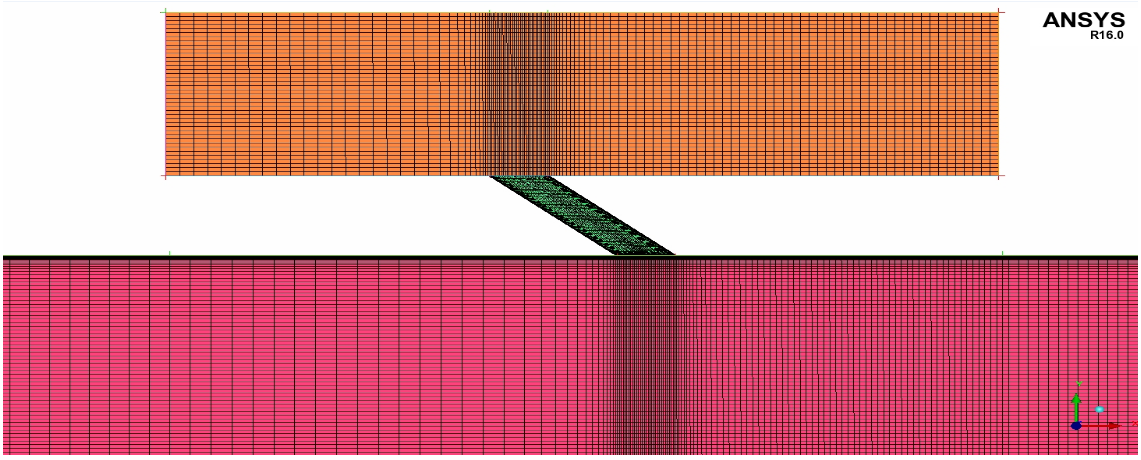

Figure 3.3: Resolved simulation mesh for hole 1.

The resolved simulations modelled the same flat plates as their corresponding point source simulations along with the cooling hole and a plenum. The plenum is extensively used in flat plate simulations[8]. The cooling hole inlet geometry and flow quantities are not necessarily known. Therefore, a plenum is used and its total pressures is varied to match the mass flow rate through the cooling hole. The plenum was set to the following boundary conditions; $P_0 = 1.02$ times the inlet total pressure and T_0 =0.61 times the inlet total temperature for hole 1 and P_0 =1.006 times the inlet total pressure and T_0 =0.61 times the inlet total temperature for hole 2. The cooling hole wall surfaces were set to no-slip and the remaining boundary conditions remained the same.

3.3 Turbine

This section gives the complete methodology used for simulating the turbine with and without film cooling.

3.3.1 Geometry

As mentioned in the introduction section, the turbine is a 1½ stage HPT. It consists of 40 NGVs, 60 rotor blades and 20 IPVs. The simulation domain consisted of 2 NGVs, 3 rotor blades and 1 IPV. For the uncooled case, the NGV and rotor blades did not have circular fillets. They were added later for the film cooled case in order to match the experimental mass flow. These fillets were added in the meshing tool used (Table 3.3). Figures 3.4a and 3.4b, show the NGVs without and with the fillets respectively. The IPV included fillets for both uncooled and film cooled cases. The no film cooling simulations with the added fillets were not redone, as the simulations are computationally expensive. The addition of fillets reduced the total mass flow rate through the turbine (reduced throat area), but does not affect the downstream flow too much. The interest is in studying the effects of film cooling on the downstream components. A no cooled case provides a baseline to this study.

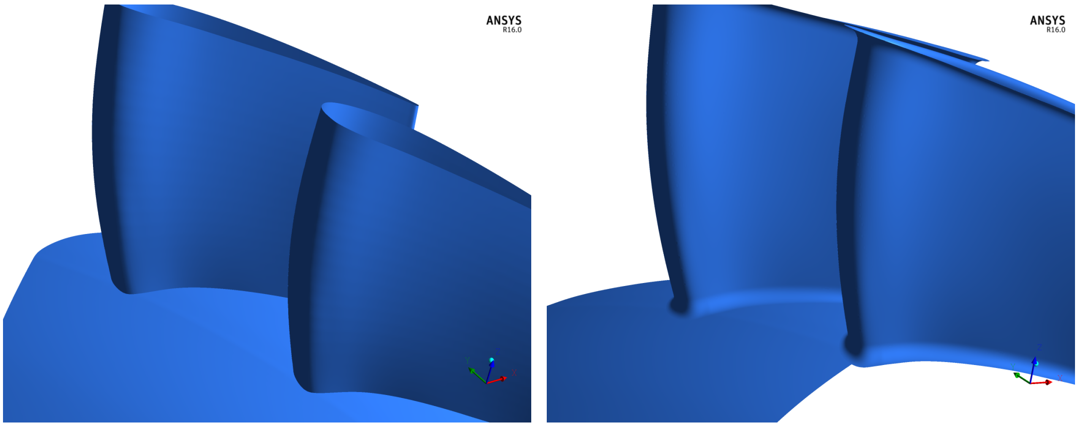

(a) Without fillets. (b) With fillets.

Figure 3.4: NGV.

3.3.2 Mesh

As mentioned in the previous subsection, fillets were added to the film cooled case. Also, the appropriate cell face size on the NGV surface needed to be set in order to get the correct momentum flux through each modelled cooling hole. Table 3.3 shows the number of cells in each of the 3 domains of the turbine for both no cooled and film cooled simulations. It also gives the y^+ range on the blade surfaces and which

Geometry		Number of cells	y^+	Meshing tool
No film cooled	NGV	7.7 million	10 - 50	G3DMESH
	Rotor	8.4 million	10 - 50	PADRAM
	IPV	1.8 million	3	ICEMCFD
Film cooled	NGV	10 million	1	G3DMESH
	Rotor	38 million	1	PADRAM
	IPV	1.8 million	3	ICEMCFD

Table 3.3: Number of cells in each domain of the turbine along with y^+ and the meshing tool used to generate the mesh.

meshing tools were used to generate the meshes. The intention was to resolve the boundary layers for heat transfer calculations as wall functions are not good enough. This meant getting the y^+ near 1. The meshes were generated at GKN Aerospace and Rolls-Royce. They were later assembled in CFXpre. The total number of cells in the no film cooling case was about 17.5 million and in the film cooled case was 50 million. The significant rise in the number of cells is due to the decrease in y^+ and the increased streamwise and spanwise node distribution. The NGV surface mesh is shown in Figure 3.5.

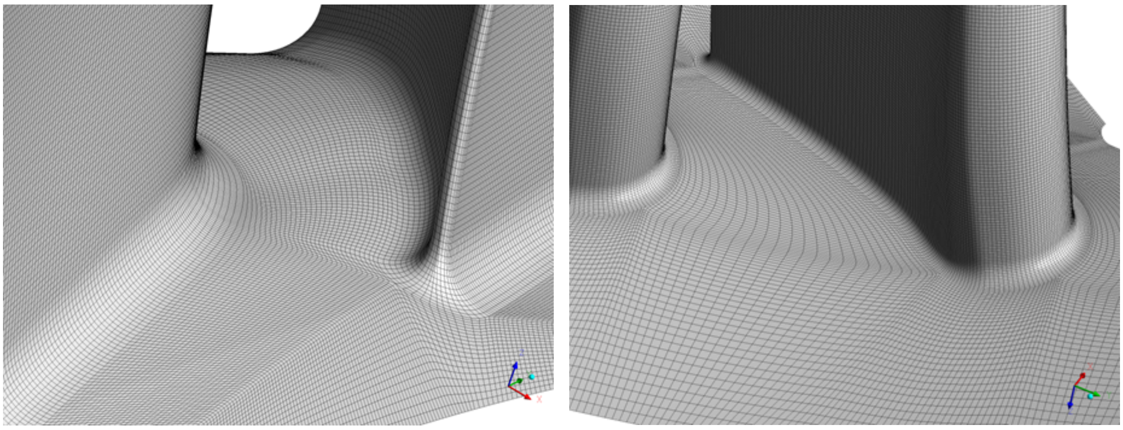

(a) Trailing edge.

(b) Leading edge.

Figure 3.5: NGV mesh for film cooled simulations.

3.3.3 Steady state simulations

Steady state simulations were performed using the multiple reference frames (MRF) mixing plane model. In reality, the NGV and IPV are stationary, while the rotor is rotating with a fixed rotational velocity in the clockwise direction (axis along the +X direction). In MRF simulations, the rotor is stationary and source terms are added to the governing equations in the rotor domain. This source term accounts for the Coriolis forces and centrifugal forces due to rotation. In this way rotation of the rotor is modelled. Mixing planes are placed between the NGV exit and rotor inlet as well as between the rotor exit and IPV inlet. Mixing planes perform circumferential averaging of all quantities, resulting in elimination of wakes and other circumferential inhomogeneities. A detailed description on MRF mixing plane model can be found in a Ph.D thesis by Petit[17]. Limitations of the mixing plane model can be found in a paper by Denton [18]. Steady state simulations are relatively quick and can be used as the initial conditions to an unsteady flow.

3.3.4 Unsteady simulations

In the unsteady simulations, the rotor domain is actually made to rotate. This results in better prediction of the flow. A sliding mesh interface is used between adjacent blade rows. This performs interpolation of values on the boundary faces where they are specified. The data is then transferred to the neighbouring patches. This method allows for the transport of wakes from upstream blades to the downstream regions. This method is essential to this study, as the influence of film cooling on the NGV, on the downstream components is of interest. More information regarding unsteady turbomachinery flows can be read in the Ph.D thesis by Petit[17].

3.3.5 Set-up and boundary conditions

The shear stress transport (SST) k-ω model was used for all the simulations. The gas is modelled as air with ideal gas properties. A uniform inlet boundary condition was used. The inlet boundary conditions was matched with the experiments and used for the film cooling case. For the no film cooling simulation, the T_0 was reduced to 0.975 times the actual inlet total temperature by doing a mass flow average of the coolant and actual total temperatures. At the outlet, the static pressure at the hub were matched with those from experiments. The radial equilibrium pressure averaging option was selected in CFX 16.0. This was done as the outlet pressure is radially increasing from hub to shroud. No-slip wall conditions were used on all the blade surfaces as well as the hub and casing surfaces. In the film cooled simulations, 2 patches on the hub surface in the rotor domain, one upstream of and one downstream of the rotor were set to free slip wall. They are coloured in green in Figure 3.6. This was done, because in reality, cavities are present and modelling these cavities is not part of the thesis. The casing in the rotor domain was set to a counter rotating wall. The hub patch downstream (coloured in yellow in Figure 3.6) was set to a counter rotating wall as well. These walls are in reality stationary. The remaining boundaries, namely the fluid regions between blade passages, were set to a rotational periodicity boundary condition.

3.3.6 Point source and cell face source methods.

As mentioned in the theory section, the point source method was initially used to model the exit of the flow through the cooling holes. In this method, the Cartesian coordinates are the locations of the cooling hole exit. CFX specifies the source terms on the cell face closest to the specified location. These cell faces need to be on the blade surface. Due to differences in the tolerances between the manufactured part and the CAD geometry, CFX does not pick the cell faces on the NGV surface. Some

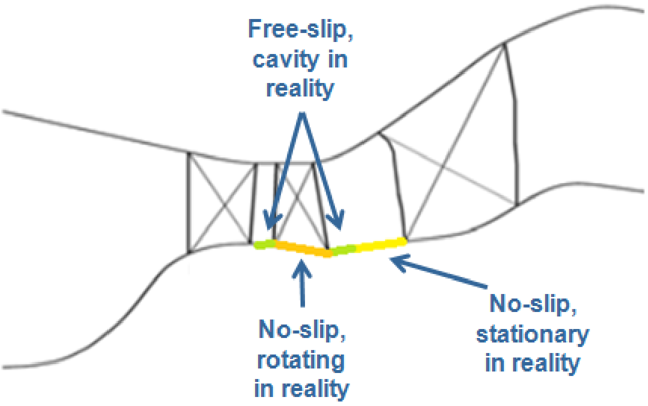

Figure 3.6: Meridional view of the turbine showing the stationary (yellow), cavities (green) and rotating (orange) parts of the rotor domain hub.

source terms end up being located on the cell faces of the cells in the boundary layer. The solve this problem, individual cell faces were picked by exporting the mesh into ICEMCFD. It must be noted that both these methods specify the source terms in the same way in CFX. Points at the location of the coolant hole exit were imported into ICEMCFD. Individual subsets of the cell faces closest to the points were picked and created. Parts from these subsets were then created. The mesh was then exported to CFX. This method is more time consuming as there are a lot of holes on each NGV. ICEMCFD takes time to create parts from subsets.

3.3.7 Fully turbulent model v/s transitional model.

The traditional two equation turbulence models used, assume that the flow is fully turbulent. However, laminar, transitional and fully turbulent boundary layers have significantly different heat transfer coefficients which makes the use of transitional turbulence models important for heat transfer calculations. More on transitional models can be found in A. Sveningsson[2]. In this thesis, the $\gamma - \theta$ transitional model available in CFX 16.0 was used. The differences in results obtained from the traditional 2 equation turbulence model and this transitional model was compared to see if the results obtained were significantly different to consider using this transitional model. This transitional models take more time to run as they need to solve 2 more variables, γ and θ. The results for this section is discussed in Appendix A.

4

Results and Discussions

This section discusses the results obtained from the flat plate simulations as well as the results from the no-cooling and film cooling simulations.

4.1 Flat plate simulations

The main aim of these flat plate simulations is to find the most suitable cell face size on which the source term will be specified. This subsection gives the results obtained from the two cooling holes selected. As mentioned in Section 3, the source term model is compared to the fully resolved cooling hole simulation. It must noted that all the conclusions made in this section are based only on visual evaluation of the results.

4.1.1 Hole 1: Resolved v/s source term cooling hole simulations

Figure 4.1 shows the temperature and Mach number contours in the meridional cut-plane, between x/D of 0 and 65, for the various cell sizes chosen and the fully resolved simulation. It should be noted that all the temperature plots in this section are normalized using the inlet total temperature. What is immediately noticeable is that on decreasing the cell size, the jet penetration increases. Case 1 (4.1a) has a low mesh density and hence a low jet penetration. Whereas, Case 3 (4.1c) has a high mesh density and hence a high jet penetration. In order for the mass flow rate to be constant, for a change in the area, in this case given by the cell face size, the velocity will change. Hence, higher density meshes will have higher velocities, increasing the jet penetration.

Case 2 (4.1b) and case 3 (4.1c) have the same mesh densities, but in case 2, the source term is divided equally amongst 4 neighbouring cells. The mass flow rate specified at each cell face is therefore reduced by a factor of 4. This reduces the velocity and hence the jet penetration. Case 4 (4.1d) has similar jet penetration to the fully resolved case (4.1e).

The Mach number contours shown in Figure 4.1 do not show any significant variation between the coolant and free stream velocities. Only case 3 shows a slightly higher coolant velocity near the cooling hole (coloured in yellow). This is because the coolant has a very low velocity in comparison to the free stream flow. Also, it has a lower temperature, lowering the value of speed of sound in it. This results in similar Mach numbers.

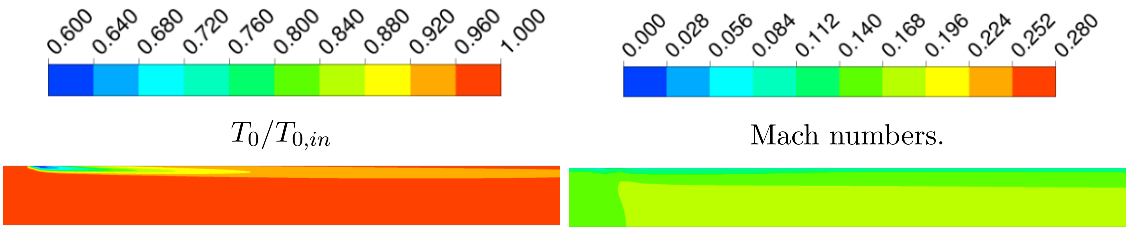

(a) Case 1.

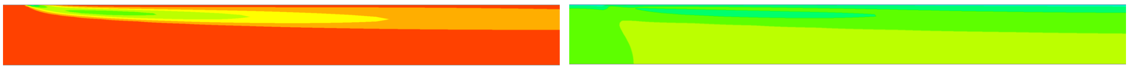

(b) Case 2.

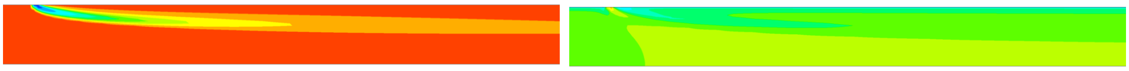

(c) Case 3.

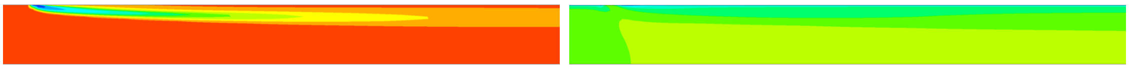

(d) Case 4.

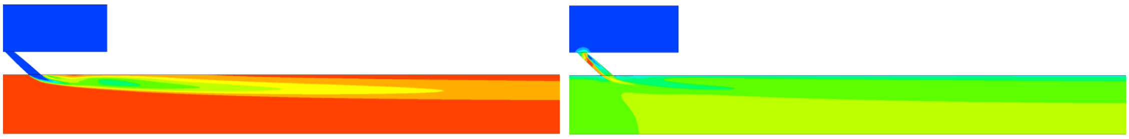

(e) Resolved case.

Figure 4.1: $T_0/T_{0,in}$ and Mach Number contours in a meridional cut-plane (0 < x/D < 65).

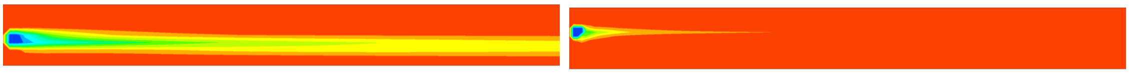

(a) Case 1. (b) Case 2.

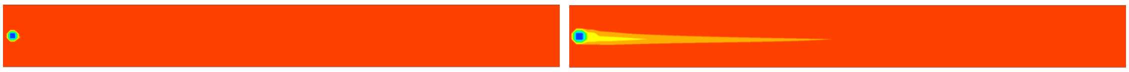

(c) Case 3. (d) Case 4.

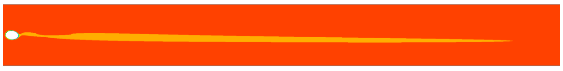

(e) Resolved.

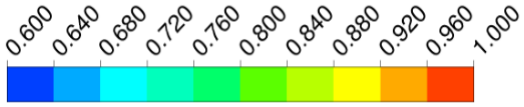

Figure 4.2: $T/T_{0,in}$ contours on the plate (0 < x/D < 65).

In Figure 4.2, none of the 4 cases predict the temperatures correctly on the surface of the flat plate. However, in this thesis, the interest is not in studying the flow and heat transfer on the NGVs. The interest is in studying the effect of the coolant on the downstream components. Predicting plate temperatures accurately, may not be important to do this.

Case 1 has the lowest temperatures on the flat plate, whereas case 3 has the highest. In the theory section, how the amount of jet penetration affects the surface temperatures was discussed. These simulations seem to agree with it.

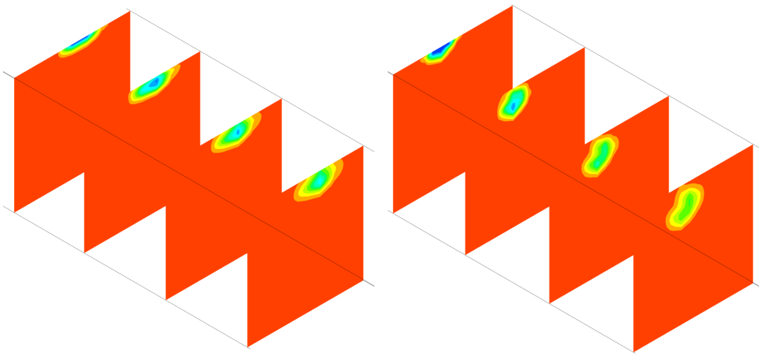

(a) Case 1. (b) Case 2.

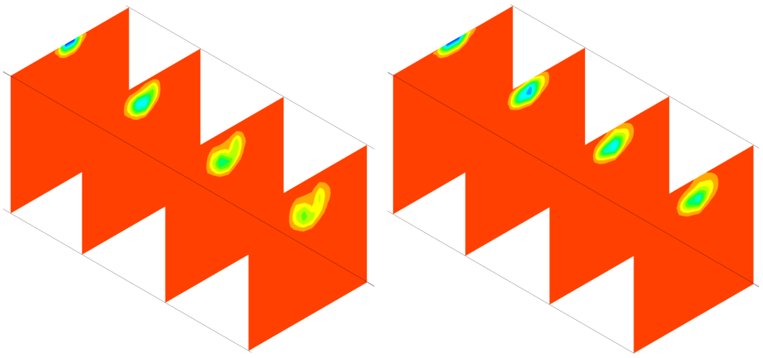

(c) Case 3. (d) Case 4.

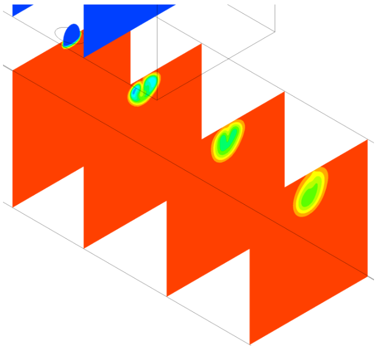

(e) Resolved.

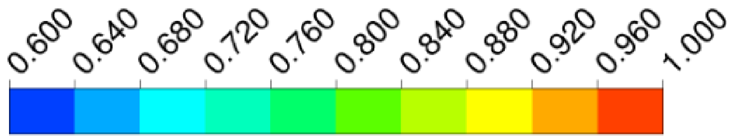

Figure 4.3: $T_0/T_{0,in}$ contours at cut-planes x/D = 0, 5, 10, 15.

In Figure 4.3, close to the hole exit, none of the source term models predict the temperatures properly. This is because the flow at and around the cooling hole is very complex. As discussed in the theory section, the flow separates on entering the cooling hole. This creates a high speed jet as the area available for the coolant to flow is reduced. In Figure 4.1, these two regions can be seen. The red colour shows the high speed jet. The blue region right next to, in the cooling holes, depicts the separated region. In Figure 4.3e, 2 counter rotating vortices at x/D = 5 can be seen. These vortices, are formed in the cooling hole, due to the flow separating at its inlet. It is then transported downstream by the main flow. Moving further downstream, the coolant mixes with the main flow. At x/D =15, for the fully resolved simulations, a more uniform temperature profile can be seen. Case 4 best resembles the resolved simulations at x/D =15. At the outlet plane, case 4 comes closest to the fully resolved simulations. This can be seen in the temperature contours in Figure 4.4.

Based on these results, case 4 is selected as the mesh size for the next cooling hole simulation. This case is then compared with the fully resolved case for a different cooling hole.

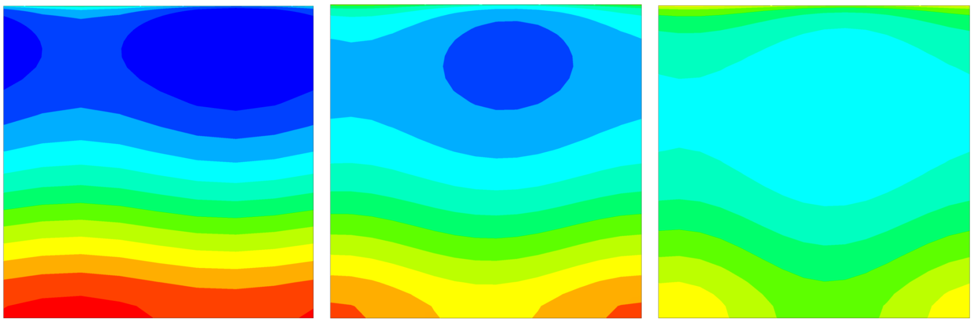

(a) Case 1. (b) Case 2. (c) Case 3.

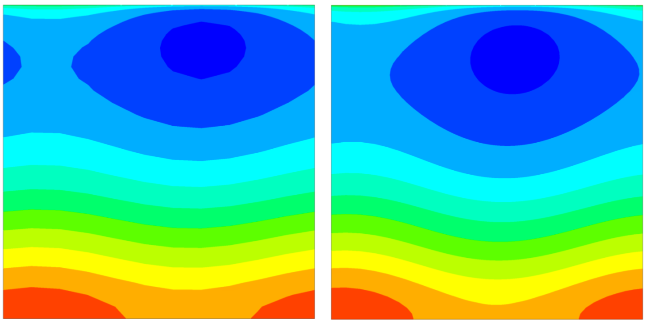

(d) Case 4. (e) Resolved.

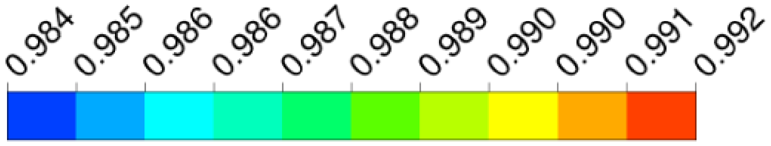

Figure 4.4: $T_0/T_{0,in}$ at the outlet.

4.1.2 Hole 2: Resolved v/s source term cooling hole simulations

The main purpose of this section, is to verify if the size of the face cell size selected gives consistent results. From Figure 4.5, the jet penetration is higher for the resolved simulation than the source term simulation. In the theory section, how higher inclined cooling holes give higher jet penetration due to coolant separation at the plate surface and due to higher vertical components of velocity with respect to horizontal components, was discussed. This is the reason for the slight difference in jet penetration. Note that the cell face size selected is calibrated for hole 1. The flat plate temperatures, shown in Figure 4.6, vary as well. It is consistent with the amount of jet penetration as well as with the theory discussed in section 2.

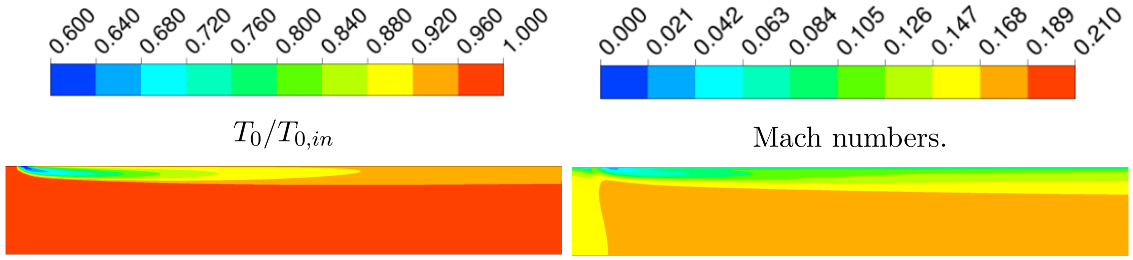

(a) Source term model.

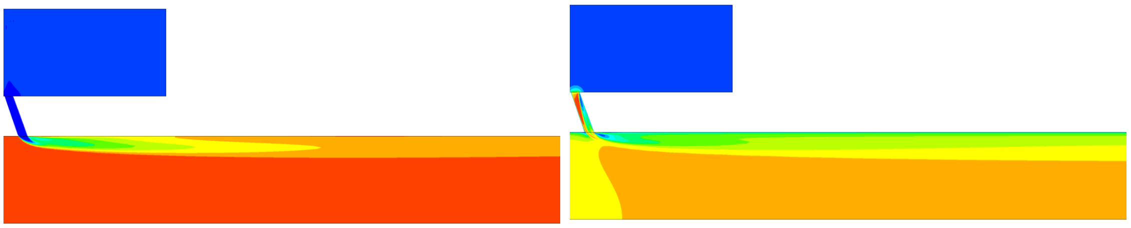

(b) Resolved simulation.

Figure 4.5: $T_0/T_{0,in}$ and Mach Number contours in a meridional cut-plane (0 < x/D < 60).

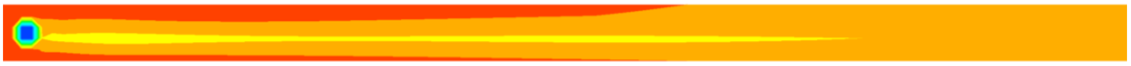

(a) Point source method.

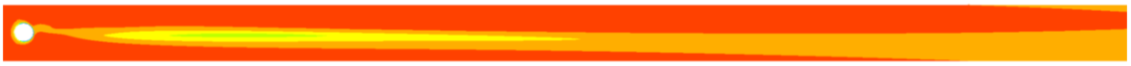

(b) Resolved.

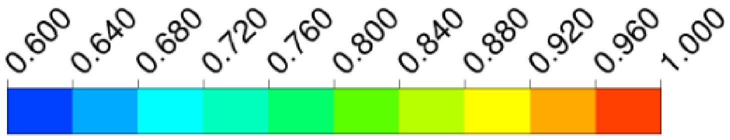

Figure 4.6: $T/T_{0,in}$ contours on the plate (0 < x/D < 60).

Figure 4.7, shows the temperatures at x/D = 0, 5, 10, 15. 2 counter rotating vortices near the cooling hole exit can be seen. At x/D = 15, the temperatures, in the case of the resolved simulations is distorted to one side. This distortion is due the higher inclination of the cooling hole with the XY-plane in comparison with hole 1. This creates one stronger counter rotating vortex with respect to the other.

This distortion is not yet dissipated into the main flow and needs to be transported further downstream to become uniform. Figure 4.8, shows the temperatures at the outlet plane. The temperatures are very similar.

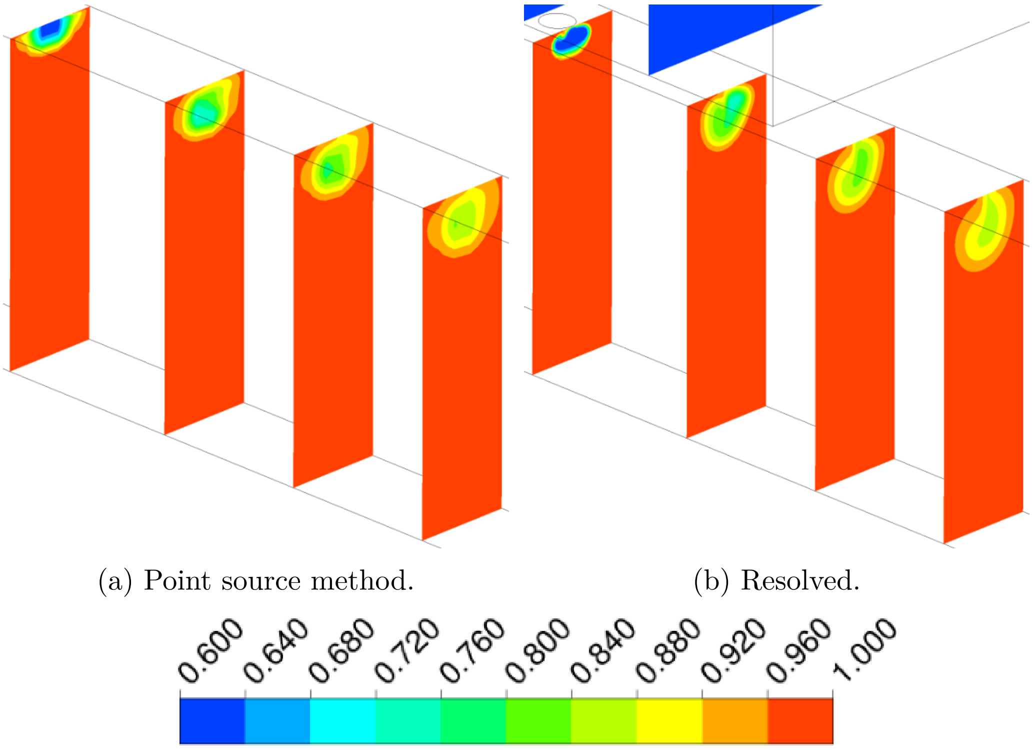

(a) Point source method.

(b) Resolved.

Figure 4.7: $T_0/T_{0,in}$ contours at x/D = 0, 5, 10, 15.

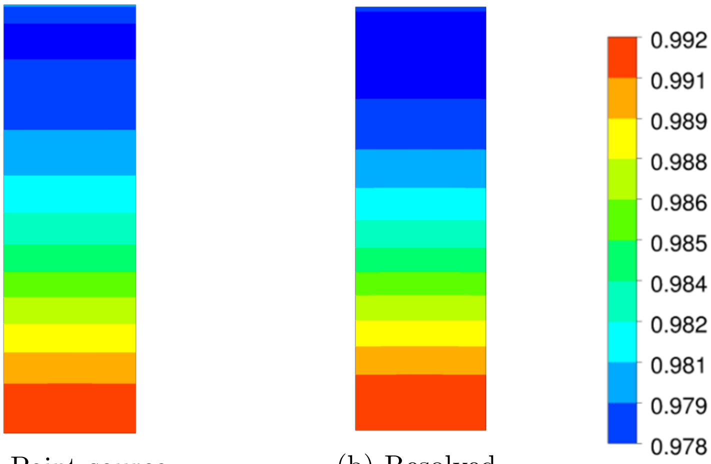

(a) Point source.

(b) Resolved.

Figure 4.8: $T_0/T_{0,in}$ contours at the outlet.

The results for cooling hole 2 seems to match well with the resolved simulation at the outlet. The jet penetrations, coolant structure at x/D=15 do not match as well with the resolved simulations as cooling hole 1. But they satisfy the basic needs. As mentioned before, the interest is in studying the effect of film cooling on the downstream components. These analysis were done to select an appropriate cell size and not to get into a detailed analysis of flat plate simulations. This cell size was set as the NGV surface cell size in order to do film cooling simulations with the point source term model available in CFX 16.0.

4.2 Turbine simulations.

This section consist of results from 4 different simulations namely; no cooling steady and unsteady as well as film cooled steady and unsteady. As mentioned in the methods section, the inlet total temperature was reduced for the no cooling simulations. How significantly the aerodynamic and heat transfer results differed in the IPV domain when film cooling was included on the NGVs versus just reducing the inlet total temperature, was assessed. Unsteady simulations for both these cases were done to look for any differences arising due to unsteady effects.

4.2.1 Pressures and temperatures on the IPV surface.

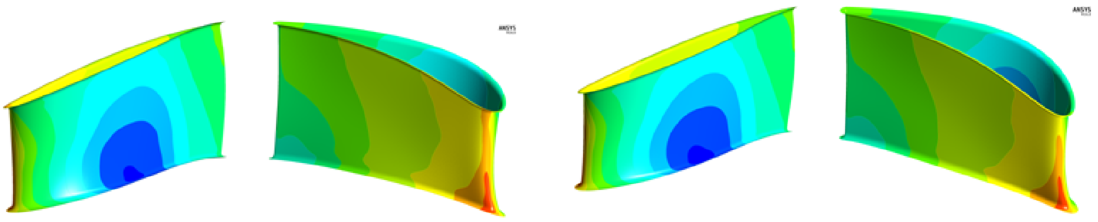

(a) Steady, no cooling, $P/P_{0,in}$.

(b) Unsteady, no cooling, $P/P_{0,in}$.

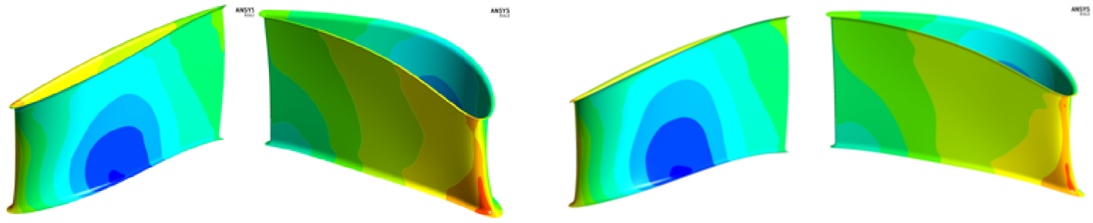

(c) Steady, film cooled, $P/P_{0,in}$.

(d) Unsteady, film cooled,$P/P_{0,in}$.

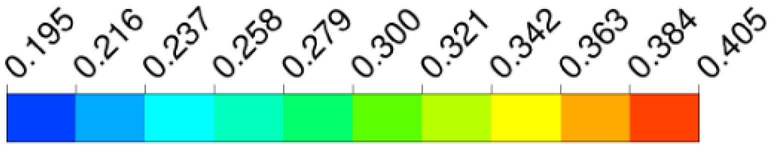

Figure 4.9: $P/P_{0,in}$ on the IPV surface.

Temperatures and pressures on the IPV surface are first looked at. From Figure 4.9, no significant differences in pressures can be seen. The leading edge(coloured in orange and red) has the highest pressures due to flow stagnation. The suction side has the lowest pressures and is coloured in dark blue.

Looking at 4.10, large variation in temperatures on the surface of the IPV near the casing, can be seen. The film cooled cases appear to have higher temperatures near the casing. Note that the no cooled simulations have lower inlet T_0 than the film cooled simulations. It is this difference in the inlet boundary condition that is showing higher temperatures on the IPV near casing for the film cooled case. The coolant is not heating up this region. The orange and red contours in 4.10c and 4.10d show these higher temperatures. They are absent in Figure 4.10a and 4.10b. There is also a variation between the steady and unsteady cases for both no film cooled and film cooled simulations. In the case of no film cooling, the temperatures on the IPV, near the casing , for the steady state are higher on the pressure side and lower on the suction side, in comparison to the unsteady case. For film cooled case, the unsteady has higher temperature on the leading edge and the suction side and lower temperatures on the pressure side, close to the trailing edge, near the casing in comparison to the steady simulation.

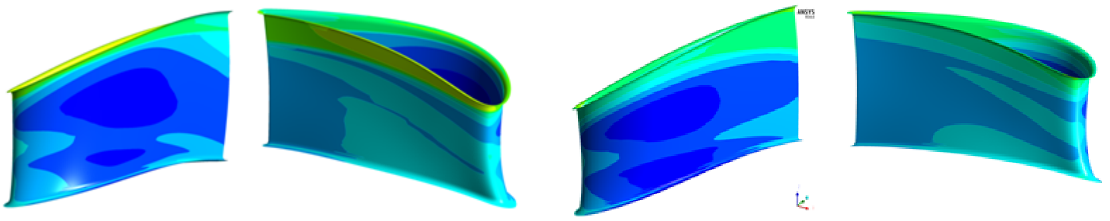

(a) Steady, no cooling, $T/T_{0,in}$.

(b) Unsteady, no cooling, $T/T_{0,in}$.

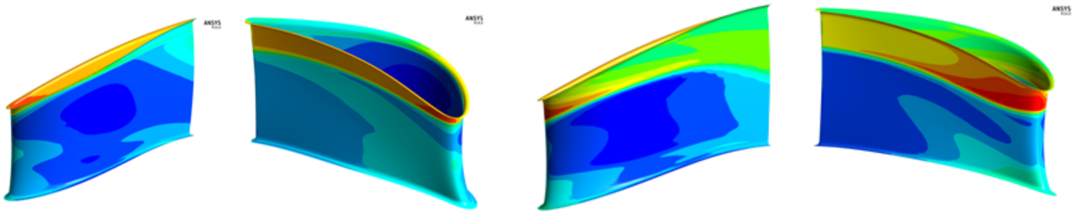

(c) Steady, film cooled, $T/T_{0,in}$.

(d) Unsteady, film cooled, $T/T_{0,in}$.

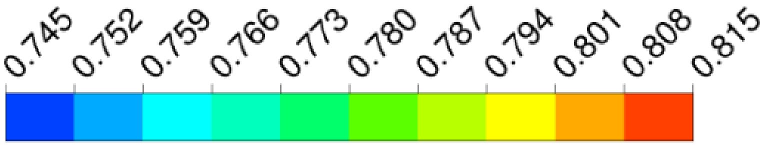

Figure 4.10: $T/T_{0,in}$ on the IPV surface.

4.2.2 Rotor inlet

To explain these variations in temperatures on the surface of the IPV, P_0 and T_0 at the rotor inlet is looked at first. Losses in the flow can be seen in the P_0. Low P_0 in the wakes of the NGV in Figure 4.11a and 4.11c can be seen. For the film cooled case (Figure 4.11c) however, the wake is wavy. This wavy structure is due to the extra losses associated with mixing of the coolant and core flows. The lower T_0 in Figure 4.11d shows the cold streaks from the coolant, in the same location i.e in the wakes of the NGVs. These cold streaks are absent in 4.11b. Note that, in a stator, no work is extracted and hence the T_0 does not change. For steady state simulations, a mixing plane is placed between the NGV and rotor domain. This mixing plane performs circumferential averaging of flow quantities, resulting in elimination of wakes and other circumferential non-homogenities. For both the steady and unsteady T_0 contours in Figures 4.11f and 4.11d respectively, the temperatures are higher near the casing. This is due to a lack of coolant on the NGVs near casing as the number of cooling holes are lower at this location. This could be a possible explanation for higher temperatures on the IPV surface near the casing.

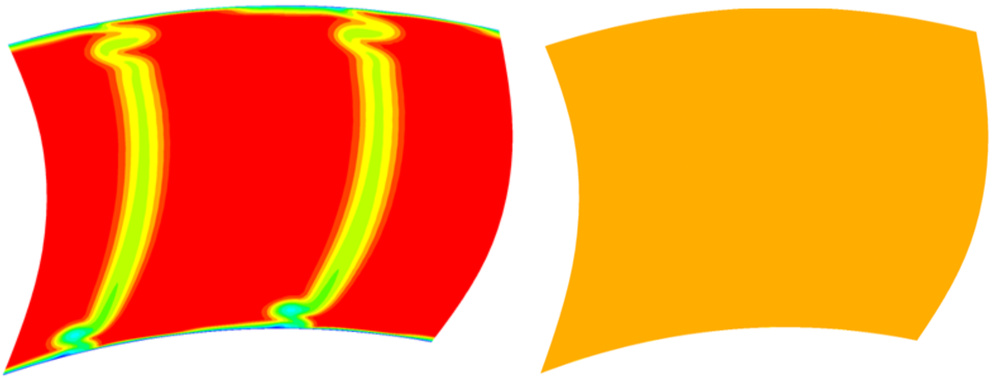

(a) Unsteady, no cooling, $P_0/P_{0,in}$ (b) Unsteady, no cooling, $T_0/T_{0,in}$.

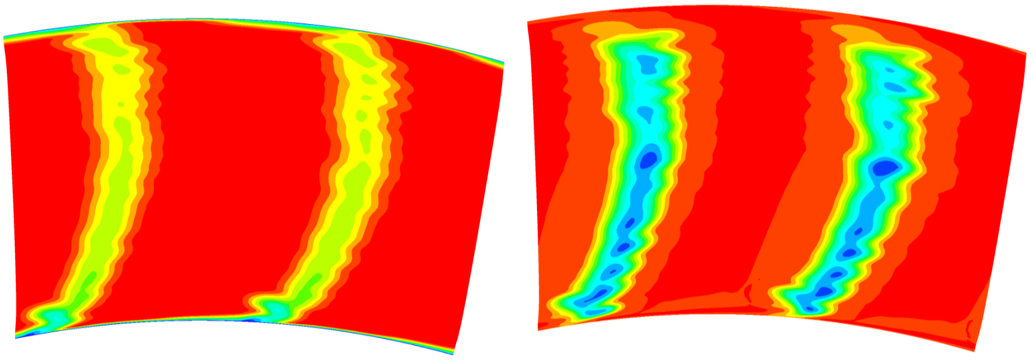

(c) Unsteady, film cooled, $P_0/P_{0,in}$. (d) Unsteady, film cooled, $T_0/T_{0,in}$.

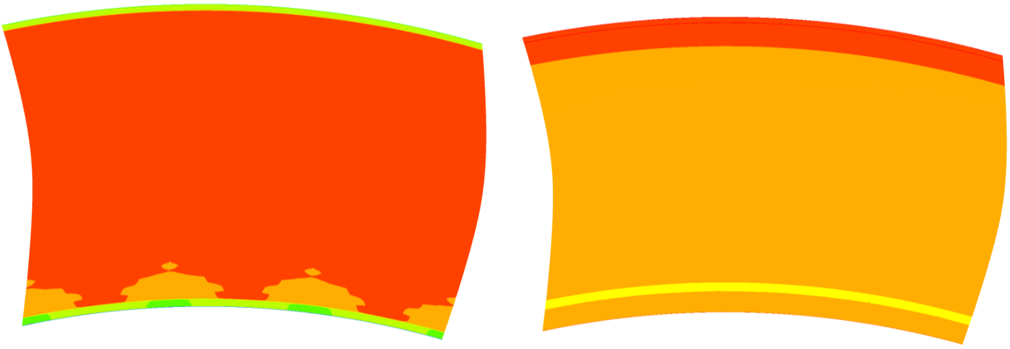

(e) Steady, film cooled, $P_0/P_{0,in}$ (f) Steady, film cooled, $T_0/T_{0,in}$.

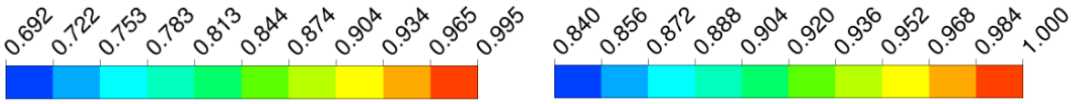

Figure 4.11: $P_0/P_{0,in}$ and $T_0/T_{0,in}$ at rotor inlet.

4.2.3 Flow features in the rotor

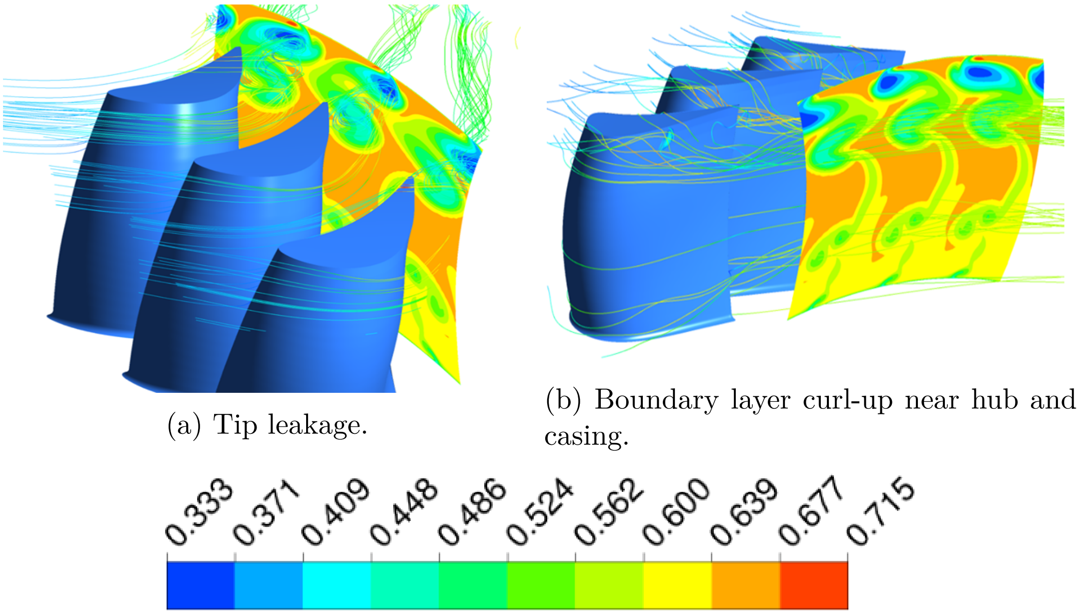

(a) Tip leakage.

(b) Boundary layer curl-up near hub and casing.

Figure 4.12: Streamlines showing vortex formation.

The flow inside a rotor is complex. Figure 4.12 shows three distinguishable vortices being formed per rotor passage. One due to the tip gap vortex, the other two are due to boundary layer curl-up near hub and casing respectively. The tip gap vortex is the strongest and is formed due to flow crossing over from the pressure side to the suction side in the tip gap. The flow near the casing migrates downwards and curls up as it leaves the trailing edge, forming a vortex just below the tip gap vortex. The flow near the hub migrates upwards and results in a vortex similar to the previous one, but it is weaker in strength. These flow features are important for understanding the flow in the IPV.

4.2.4 IPV inlet in the relative frame of reference.

Figure 4.13c shows higher temperatures near the casing than Figure 4.13b. In the relative frame of reference, no work is extracted by the flow. Therefore the total temperatures upstream and downstream are similar. This explains the higher temperatures near the casing for the film cooled case.

In the steady case (figure 4.13a), 6 dark blue spots is noticed near the casing. 3 of these are the tip leakage vortices, while the remaining 3 are due to boundary layer curl up near the casing of the rotor. Losses due to vortex formation are seen as a drop in total temperatures in the relative frame. In a stationary frame, the losses result in higher total temperatures. This is because the expected amount of work that was supposed to be extracted from the flow, is not, resulting in lower drops in total temperatures.

The vortex losses can also be seen in the P_0 contours in Figure 4.14. The steady state case has 6 dark blue spots, whereas the time averaged unsteady has 3 light

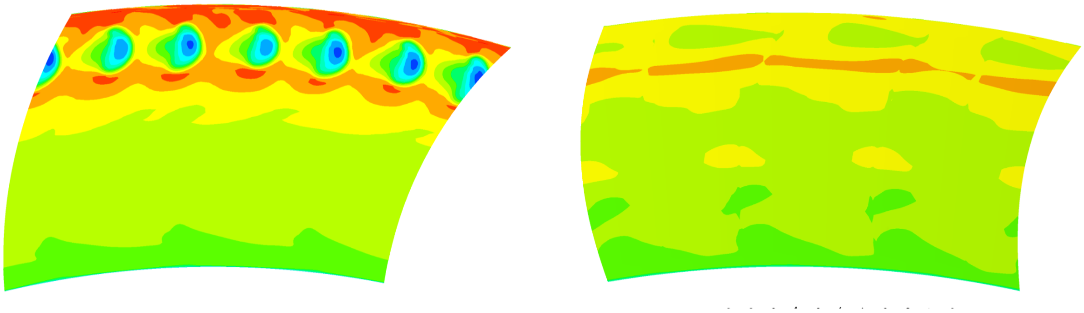

(a) Steady, film cooled.

(b) Unsteady, no cooling.

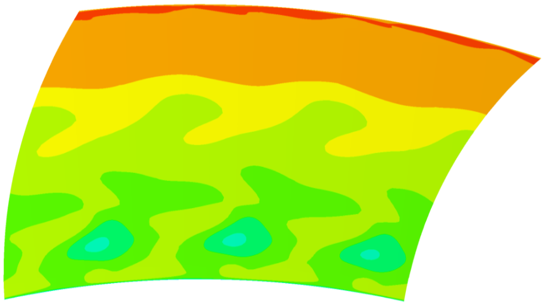

(c) Unsteady, film cooled.

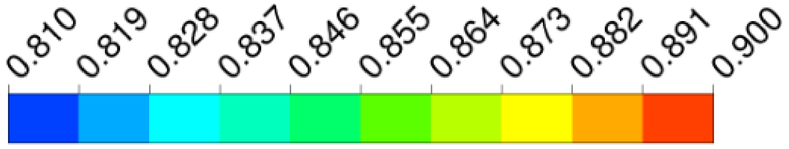

Figure 4.13: Time averaged $T_0/T_{0,in}$ at IPV inlet in the relative frame of reference.

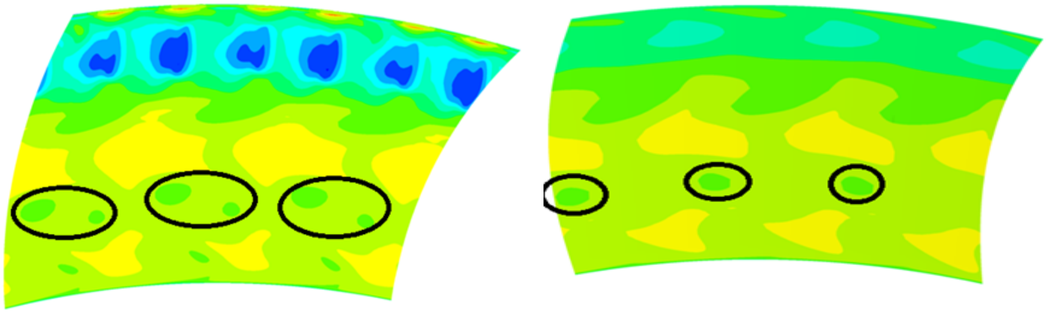

(a) Steady.

(b) Unsteady.

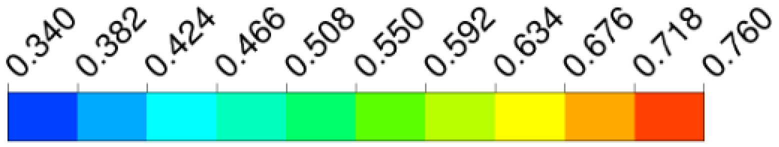

Figure 4.14: Time averaged $P_0/P_{0,in}$ at IPV inlet in the relative frame of reference.

blue spots. Also, the dark green spots, circled in black in Figure 4.14, have different number of vortices. The reason for this difference will be explained in the upcoming section.

4.2.5 Vortex formation in the rotor domain

To understand the reason for differences in P_0 contours at the IPV inlet, the P_0 contours at two different locations downstream of the rotor blades, in the relative frame of reference, for both steady and unsteady simulations, is studied. Near the trailing edge, similar levels of total pressures (Figures 4.15) is noticed. Moving further downstream, the vortices seem to dissipate much faster for the unsteady case. This can be seen by higher P_0 in 4.15d than 4.15c. This explains why the 6 dark blue spots in 4.14b is not seen. The boundary layer curl-up near the hub, for the unsteady case, has one vortex per blade. For the steady case, one vortex seems to induce another as it moves further downstream. This explains the reason for the two vortcies per blade in Figure 4.14a.

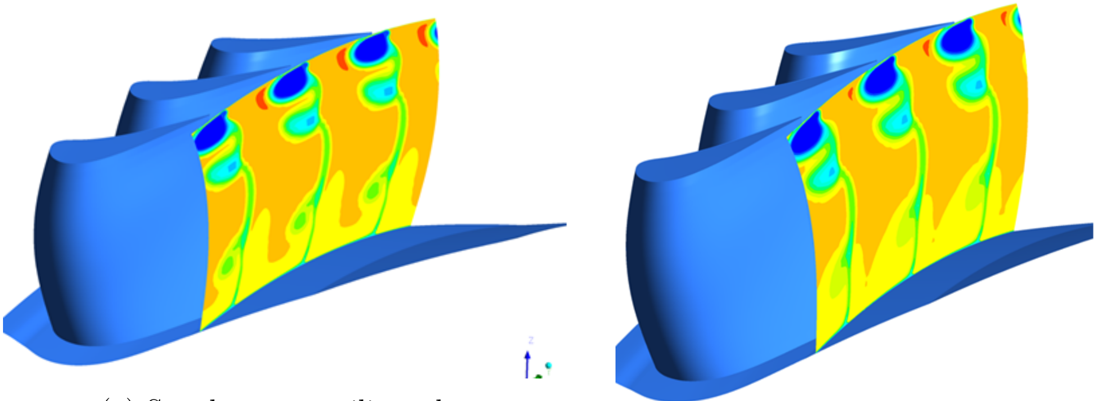

(a) Steady, near trailing edge.

(b) Unsteady, near trailing edge.

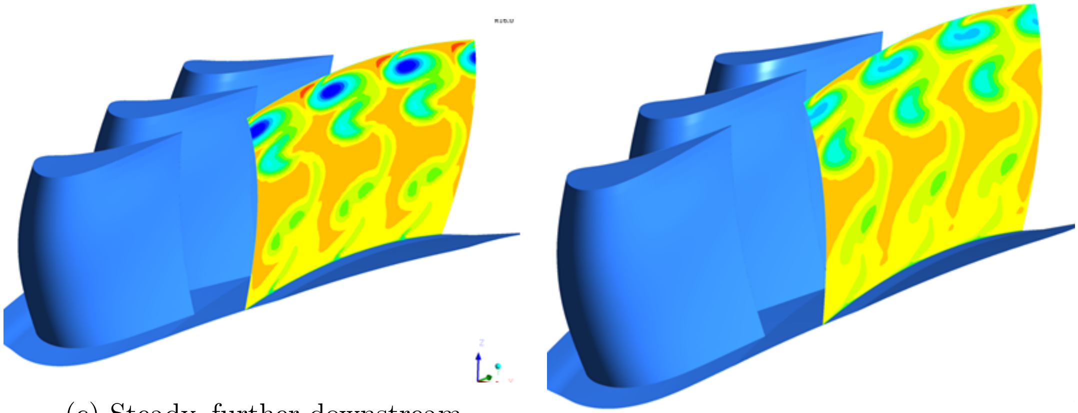

(c) Steady, further downstream.

(d) Unsteady, futher downstream.

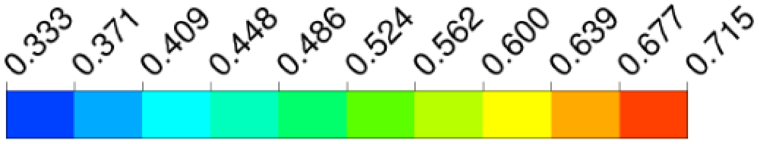

Figure 4.15: $P_0/P_{0,in}$ contours showing regions of losses.

4.2.6 IPV inlet in the stationary frame of reference.

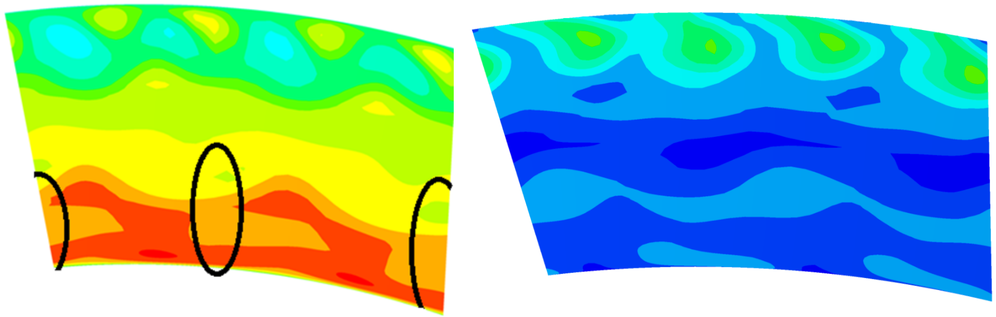

(a) No cooling $P_0/P_{0,in}$.

(b) No cooling $T_0/T_{0,in}$.

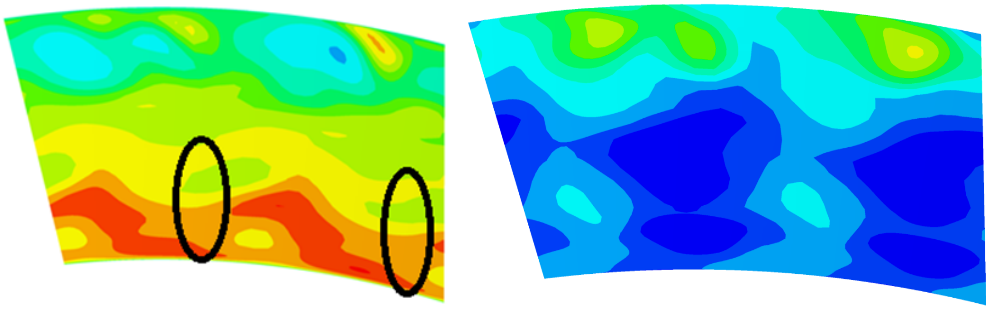

(c) Film cooled $P_0/P_{0,in}$.

(d) Film cooled $T_0/T_{0,in}$.

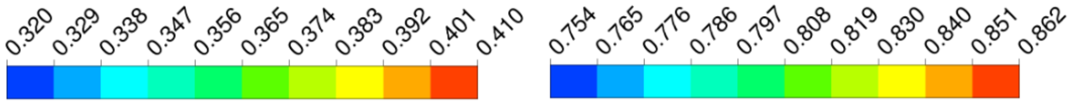

Figure 4.16: Time averaged IPV inlet $P_0/P_{0,in}$ and $T_0/T_{0,in}$.

Figure 4.16, shows the P_0 and T_0 at the inlet to the IPV for both the unsteady cases. The location of the NGV wakes are circled in black. Even though the contours are time averaged, the NGV wakes are still captured in the IPV domain. This is because the sliding mesh interface allows for the wakes to be transported downstream. The wakes can be seen as low total temperatures in Figure 4.16d. These are the cold streaks of the coolant that travel downstream along with the wakes. In steady simulations, the mixing plane mixes out the wakes. Lower total temperatures near the casing for the no cooled case is also seen.

4.2.7 Flow in the IPV domain.

Figure 4.17 and 4.18, show how the wakes from the NGVs travel downstream in the IPV domain. The orange colour is the wake region. The wakes grow larger as they move downstream due to mixing. In Figure 4.17, low P_0 (blue colour) at the inlet to the IPV can be seen. These are losses due to the the tip leakage flow. The cold streaks(dark blue) in the wake region can be seen in Figure 4.19 and 4.20. The two cold streaks, one on the pressure side and the other on the suction side, flow on both sides of the IPV and combine downstream into one. The total temperature of this cold streak in the IPV increases as it mixes out with the core flow. The red

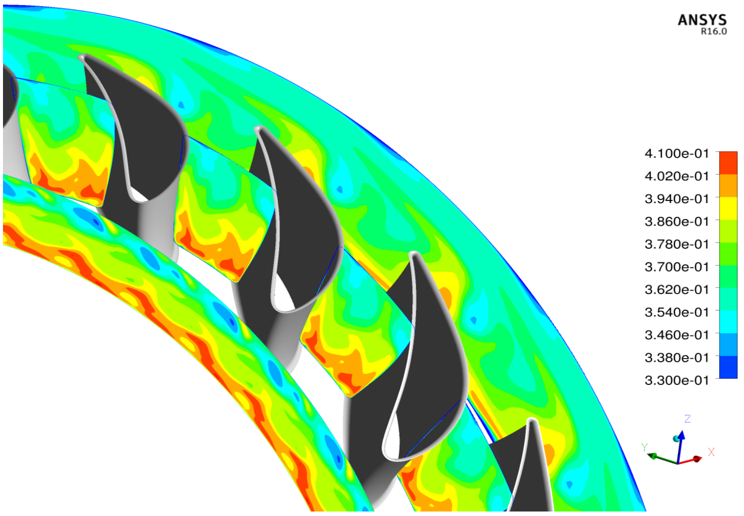

Figure 4.17: Time averaged $P_0/P_{0,in}$ at different cut-section in the IPV domain

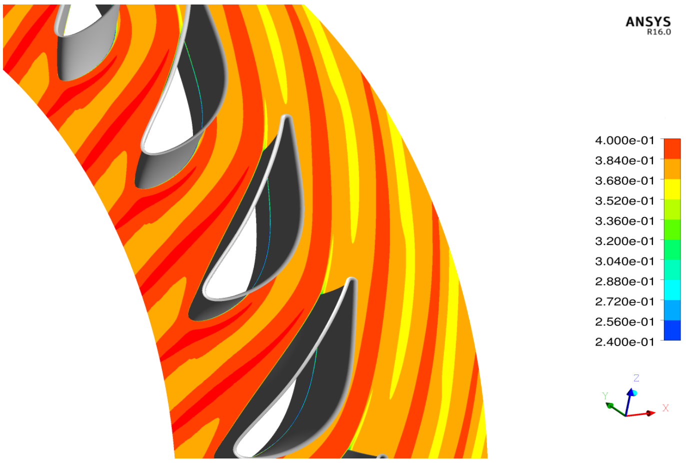

Figure 4.18: Time averaged $P_0/P_{0,in}$ at 30% span in the IPV domain

spots, at the inlet to the IPV in Figure 4.19, are due to the tip leakage vortex. As mentioned before, the total temperatures of the fluid in the tip region do not drop as much as they should, resulting in higher temperatures in these regions.

The hub and casing surface temperatures for both the unsteady cases, in the IPV domain, are shown in Figures 4.21 and 4.22 respectively. Cold and hot streaks on the hub for the film cooled case (Figure 4.21b) can be seen. The hub temperatures in the absence of cooling are more uniform (Figure 4.21a). This difference between the two cases will affect the results while calculating the heat transfer coefficients at the hub. The casing shows regions of higher temperatures due to the tip leakage vortex. The no cooled case however, has a overall lower surface temperatures at the casing. Again, this will result in different heat transfer coefficients.

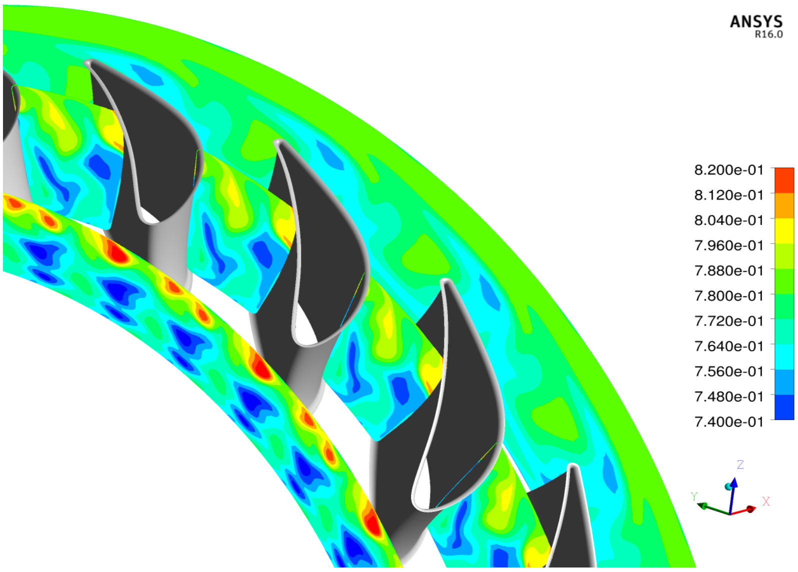

Figure 4.19: Time averaged $T_0/T_{0,in}$ at different cut-section in the IPV domain (film cooled).

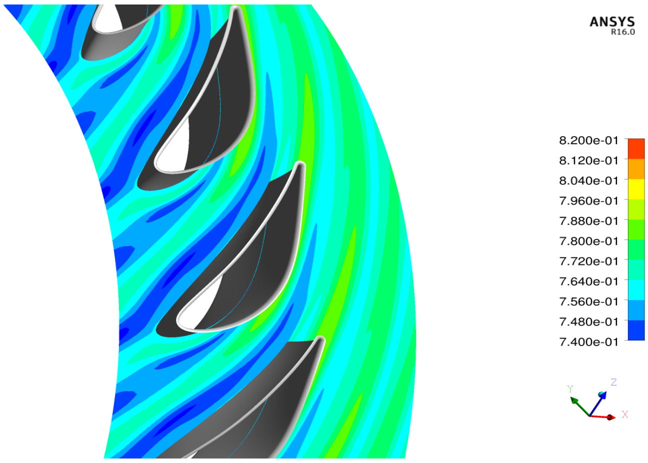

Figure 4.20: Time averaged $T_0/T_{0,in}$ at 50% span in the IPV domain (film cooled).

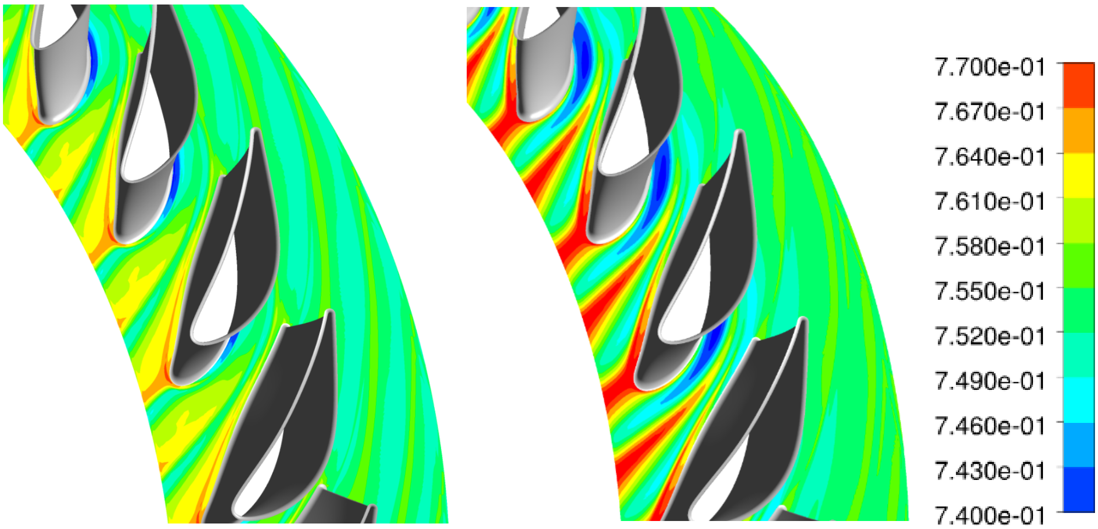

(a) No cooling.

(b) Film cooled.

Figure 4.21: Time averaged IPV hub $T/T_{0,in}$.

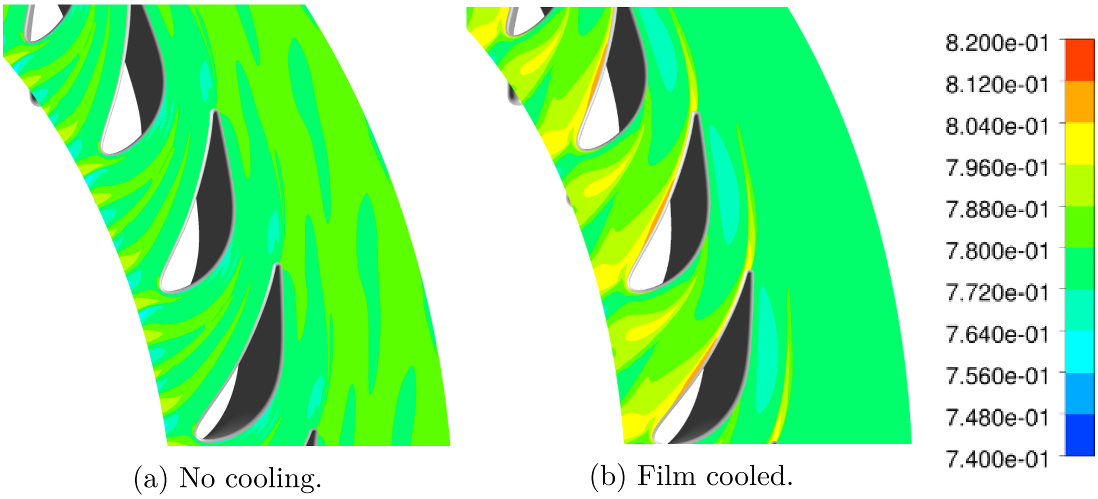

(a) No cooling.

(b) Film cooled.

Figure 4.22: Time averaged IPV casing $T/T_{0,in}$.

4.2.8 CFD v/s experimental data.

4.2.8.1 Pressure on IPV surface.

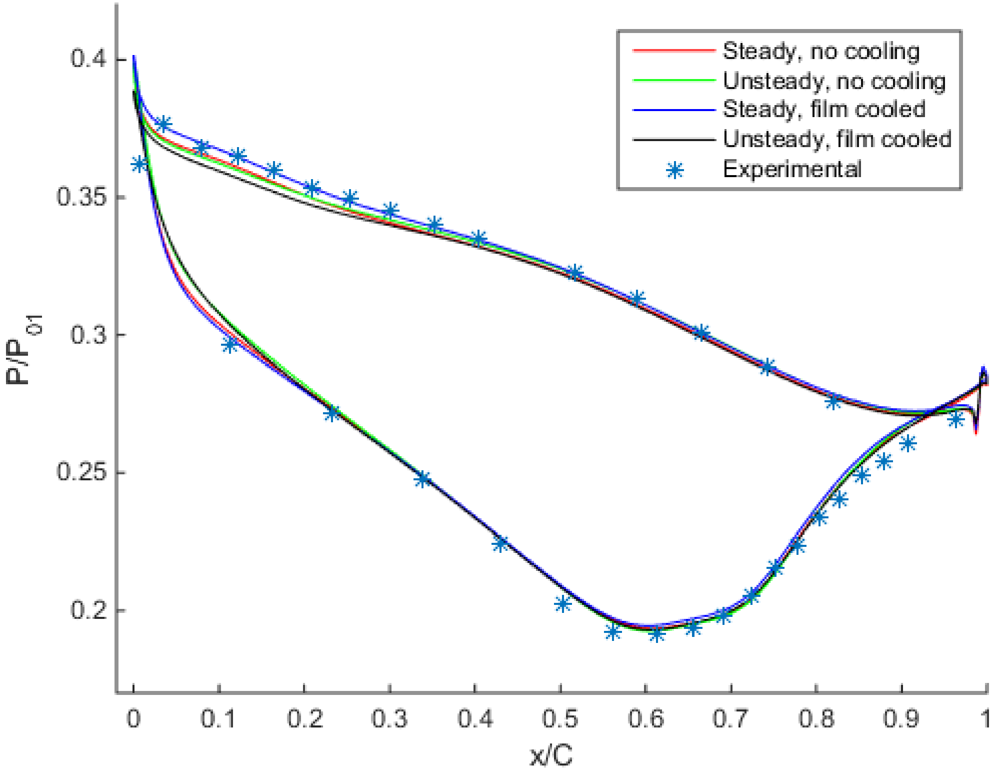

Figure 4.23: Pressures on IPV surface at 10% span.

Figures 4.23, 4.24 and 4.25 show the pressures normalized with inlet total pressure (P_{01}) at 10%, 50% and 90% spans respectively. The leading edge is at x/C = 0 and

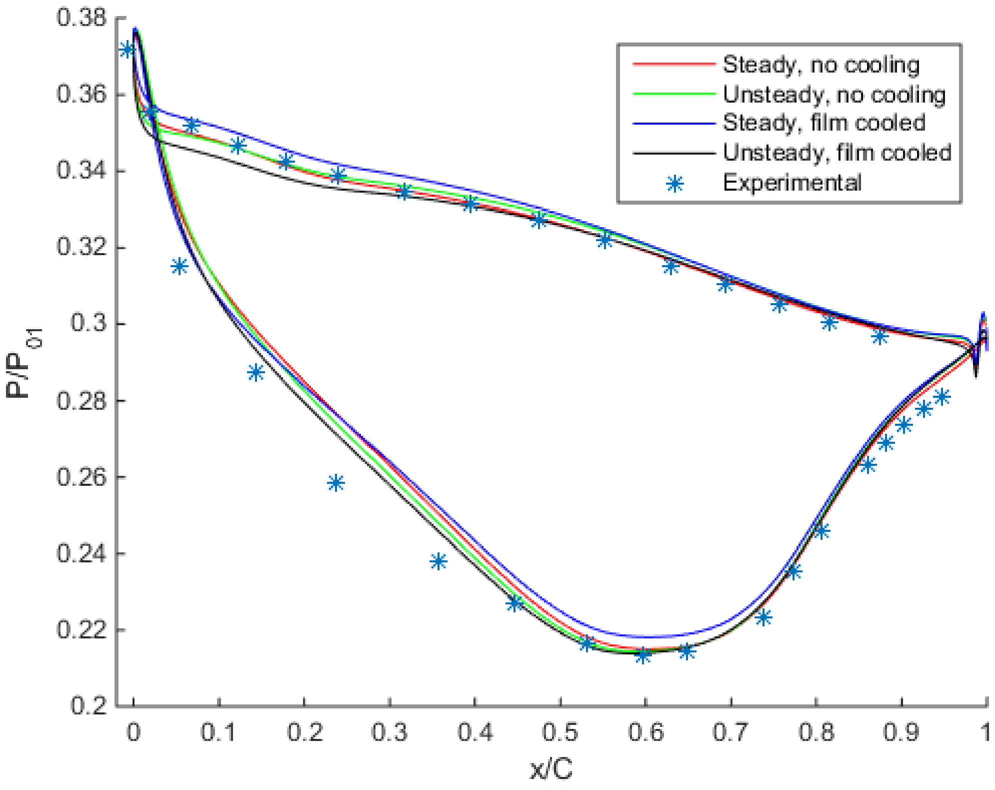

Figure 4.24: Pressures on IPV surface at 50% span.

the trailing edge at x/C = 1, where C is the chord length at that span. The pressures on the suction side are lower than those on the pressure side, as expected. The flow accelerates continuously along the entire chord on the pressure side, leading to a continuous drop in pressure. On the suction side, the flow accelerates till a chord length of about 0.6, then decelerates till the trailing edge. This can be seen by a decrease and then increase in pressures.

Both the no film cooled simulations match the experimental results the best. At the leading edge, for 50% and 90% span, the steady state film cooled simulations over-predict the pressures, while the unsteady film cooled under-predicts it with respect to the experimental data. On moving towards the casing, these trends become more pronounced. The differences arise due to varying incidence angles near the casing. For the unsteady film cooled, the incidence angles are lower near the casing, while for the steady film cooled, it is higher. The no film cooling cases, have an intermediate incidence angle. The reason for this variation needs to be analyzed properly and is not yet fully understood. A possible explanation could be the differences in tip leakage prediction in CFX. This vortex, which affects the flow near the casing, could be affecting the incidence angles. For the film cooled cases, the rotor and NGV meshes were changed. These new meshes are more dense and should resolve the tip leakage more accurately. The unsteady simulations, should also be able to predict the tip leakage vortex more accurately. This is not seen in Figures 4.24 and 4.25.

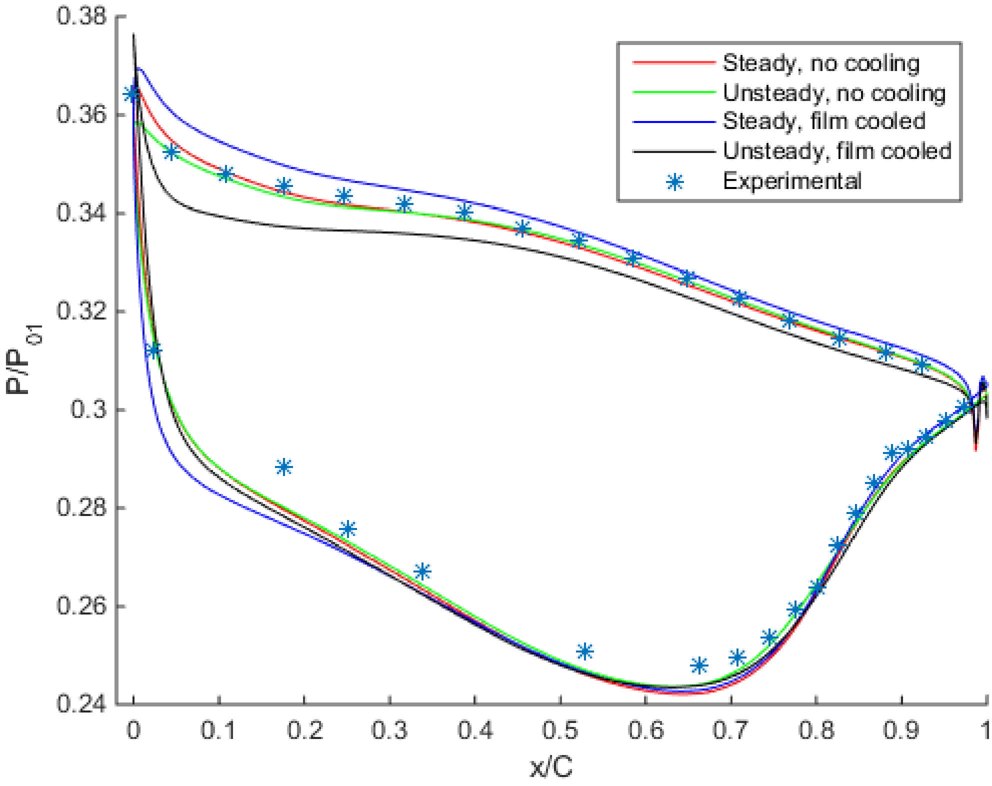

Figure 4.25: Pressures on IPV surface at 90% span.

4.2.8.2 Hub and casing pressures at different stations in the turbine.

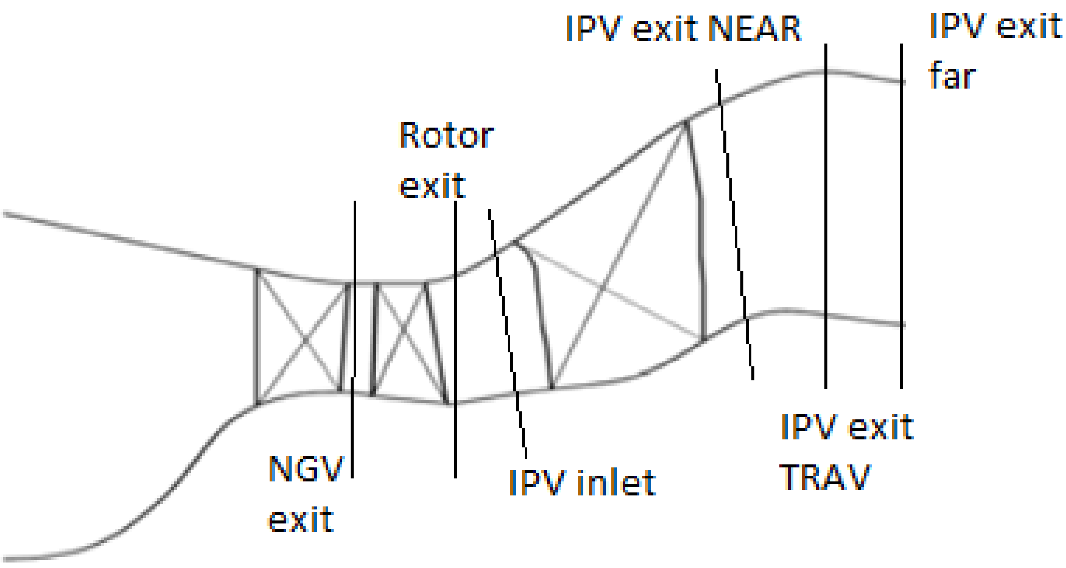
IPV exit NEAR
IPV exit
far
Rotor
exit
NGV
exit
IPV inlet
IPV exit
TRAV

Figure 4.26: Location of pressure measurements.

Pressures at different stations were measured on the hub and casing during the experiments. The location of the stations are shown in Figure 4.26. These pressures were circumferentially averaged and compared to the four turbine simulations done. Case 1 and 2 are the no film cooled steady and unsteady simulations respectively. Case 3 and 4 are the film cooled steady and unsteady simulations respectively.

Station	Experiments	Case 1	Case 2	Case 3	Case 4
NGV exit casing	0.601	0.646	0.643	0.642	0.639
NGV exit hub	0.542	0.575	0.571	0.572	0.568
Rotor exit casing	0.332	0.336	0.334	0.338	0.332
Rotor exit hub	0.344	0.356	0.356	0.36	0.355
IPV inlet casing	0.347	0.338	0.338	0.327	0.341
IPV inlet hub	0.344	0.354	0.356	0.356	0.352
IPV exit NEAR casing	-	0.296	0.296	0.296	0.295
IPV exit NEAR hub	-	0.26	0.26	0.26	0.26
IPV exit TRAV casing	0.298	0.302	0.301	0.302	0.3
IPV exit TRAV hub	0.267	0.262	0.263	0.263	0.262
IPV exit FAR casing	0.299	0.301	0.301	0.301	0.3
IPV exit FAR hub	0.264	0.264	0.264	0.264	0.264

Table 4.1: Hub and casing static pressures.

Station	Case 1	Case 2	Case 3	Case 4
NGV exit casing	7.42	6.92	6.74	6.21
NGV exit hub	6.04	5.26	5.51	4.67
Rotor exit casing	1.15	0.52	1.84	-0.02
Rotor exit hub	3.45	3.55	4.58	3.16
IPV inlet casing	-2.49	-2.42	-5.63	-1.71
IPV inlet hub	3.0	3.27	3.38	2.3
IPV exit NEAR casing	-	-	-	-
IPV exit NEAR hub	-	-	-	-
IPV exit TRAV casing	1.13	0.96	1.23	0.45
IPV exit TRAV hub	-1.61	-1.58	-1.55	-1.67
IPV exit FAR casing	0.62	0.49	0.57	0.14
IPV exit FAR hub	-0.03	-0.04	-0.03	0.05

Table 4.2: Percentage errors in hub and casing static pressures.

Table 4.1 shows values of the circumferentially averaged pressures normalized with the inlet total pressure for the experiments as well as the four CFD simulations. Table 4.2 shows the percentage error between the CFD simulations and the experiment. Moving from the steady no cooled simulations to the unsteady film cooled simulations, a reduction in the pressures errors for most of the stations is noticed. Some of these differences can be attributed to the increased mesh resolution for the film cooled simulations. The unsteady simulations show overall better predictions of pressure compared to its steady counterpart. This is because the unsteady simulations resolves the flow better and is able to account for any unsteadiness in it. It also allows for transport of wakes between interfaces, which can cause localized variations in pressures.

In Table 4.2, a large error is seen at the NGV exit location. This large error is present for all the simulations. The exact cause for this error is not known, but we think that during the experiments, there is flow ingestion at the cavity located upstream of the rotor blades. This ingestion would be affecting the pressure readings at that location during the experiments.

5

Conclusion

5.1 Flat plate simulations.

In the thesis, point sources available in CFX 16.0 were used to specify the source terms on the surface of the NGV to model the film cooling. This source term is applied on the cell face located closest to the location specified by the user. The flat plate simulations showed that the point source method is extremely mesh dependent. This is attributed to the fact that this method does not specify the momentum sources. The momentum flux is controlled by the cell face area. It was however still possible to find the correct mesh resolution to capture the downstream effect of the cooling.

5.2 Turbine simulations.

5.2.1 Aero

Examining the pressure contours on the IPV surface, no significant differences in pressures on the surface of the IPV between steady and unsteady simulations were found. It also did not seem to be affected by the film cooling of the NGVs.

Comparing the pressures with the experimental results, showed that the no film cooled simulations predicted the pressures most accurately on the IPV surface. Near the leading edge, at 50% and 90% spans, the steady film cooled simulations over-predicted the pressures, while the unsteady film cooled under-predicted it. These predictions are enhanced closer towards the casing. It is believed that the tip leakage vortex affects the incidence angles at the IPV near the casing, resulting in the differences in pressure predictions. This needs to be analyzed more in detail.

The circumferentially averaged pressure predictions on the hub and casing at different stations in the turbine improved on increasing the mesh resolution. It also improved for the unsteady simulations. This improvement is because of better resolution of the flow.

5.2.2 Heat transfer.

The temperatures on the IPV near casing are affected heavily by both the cooling scheme as well as the tip leakage. Note that the no film cooled simulations had lower inlet T_0. The absence of enough coolant near the casing of the NGVs meant that the IPV near casing temperatures are higher for the film cooling simulations. The magnitude of the tip leakage flows affects how much total temperature drop takes place through the rotor blades. Steady simulations showed larger tip leakage vortices, meaning that the temperatures at the locations of these vortices were higher. This affects the IPV near casing temperatures.

The presence of stronger cold and hot streaks on the IPV hub for the film cooled unsteady case meant that the temperature distribution on the hub differed significantly from the no film cooled unsteady case. This difference would significantly affect the hub heat transfer.

The IPV casing saw lower overall temperatures for the no film cooled unsteady case in comparison to the film cooled unsteady case. This difference would impact the casing heat transfer.

5.3 Future work.

The reason for significant differences in pressures at the IPV leading edge near casing needs to be analyzed more in detail. The variation of pressures circumferentially in the IPV domain needs to be validated with experimental data. The experimental data was not provided during the thesis as the experiments are still underway.

This thesis does not include heat transfer calculations. To verify the accuracy of the simulations, the heat transfer data needs to be extracted and compared with experimental data. The experimental data required for this comparison was not available at the time of this thesis.

The current simulations are done with a uniform inlet boundary condition. Experiments including a combustor simulator are already planned as part of the LEMCOTEC project. CFD studies of this additional configuration that would allow for CFD validation of the effect of the combustor are also planned. The swirl from the combustor is expected to significantly affect the flow in the IPV domain. This would also impact the heat transfer in the IPV domain as well.

Correlations to model the structure of the coolant at the exit of the cooling holes on the NGVs could be developed and implemented in the CFD tools. This correlation would need to capture the effect of the flow through the cooling holes more accurately and would also need to account for the spanwise and streamwise variation of the coolant on the NGVs. This model should be able to give more accurate heat transfer data as well.

Bibliography

[1] The Jet Engine, Rolls-Royce, 2005.

[2] A. Sveningsson, Transitional modelling - a review, Chalmers University of Technology, Gothenburg, Sweden, January 17, 2006.

[3] S. L. Dixon, C. A. Hall, Fluid Mechanics and Thermodynamics of Turbomachinery, 7th Edition, Butterworth-Heinemann, 2014.

[4] http://www.soue.org.uk/souenews/issue7/osney.html

[5] D. J. Denton, Loss mechanisms in turbomachines, Journal of Turbomachinery, 115, 621-656 (1993).

[6] P. Dahlander, Source term model approaches to film cooling simulations, Ph.D thesis, Chalmers University of Technology, Gothenburg, Sweden (2001).

[7] H. I. H. Saravanamuttoo, G. F. C. Rogers, H. Cohen, P. V. Straznicky, Gas Turbine Thoery, 6th Edition, Pearson Education Hall, 2009 .

[8] T. G. auf dem Kampe, S. Völker, A correlation-based methodology to predict the flow structure of flows emanating from cylindrical holes with application to film cooling, Heat Transfer Research, Vol. 41, No. 6 (2010).

[9] A. Bradley, Prediction of vane film cooling in gas turbines: Correlations and parameters, Report, Linköping Institute of Technology, Linköping, Sweden.

[10] S. Baldauf, Filmkühlung thermisch höchstbelasterter Oberächen: Korrelation thermographischer Messungen, Ph.D thesis, University of Karlsruhe (2001).

[11] S. Baldauf, M. Scheurlen, Correlation of film cooling effectiveness from thermographic measurements at engine like conditions, In ASME Turbo Expo 2002, Heat Transfer, Manufacturing Materials and Metallurgy.

[12] M. Plesniak, Noncanonical Short Hole Jets-in-Crossflow for Turbine Film Cooling, Journal of Applied Mechanics, 73(3), 474-482, Sep 26, 2005.

[13] C. Saumweber, A. Schulz, Free-Stream effects on the cooling performance of cylindrical and fan-shaped cooling holes, In ASME Turbo Expo 2008, Heat Transfer, Manufacturing Materials and Metallurgy.

[14] T. G. auf dem Kampe, F. N. Zehe, S. Völker, A model for cylindrical hole film cooling: Part 1 - A correlation for jet-flow with application to film cooling, In proceedings of the ASME Turbo Expo 2010: Power for Land, Sea and Air, no. GT2010-22787.

[15] T. G. auf dem Kampe, S. Völker, A model for cylindrical hole film cooling: Part 2, Model formulation, implementation and results, In proceedings of the ASME Turbo Expo 2010: Power for Land, Sea and Air, no. GT2010-22788.

[16] C. Langowsky, D. T. Vogel, Influence of film cooling on the secondary flow in a turbine nozzle, AIAA Journal, Vol. 35, No. 1, January 1997.

[17] O. Petit, Towards full predictions of the unsteady incompressible flow in rotating machines using openfoam, Gothenburg, Sweden (2012).

[18] D. J. Denton, Some limitations of Turbomachinery CFD, In proceedings of the ASME Turbo Expo 2010: Power for Land, Sea and Air, GT2010.

A

Transitional model.

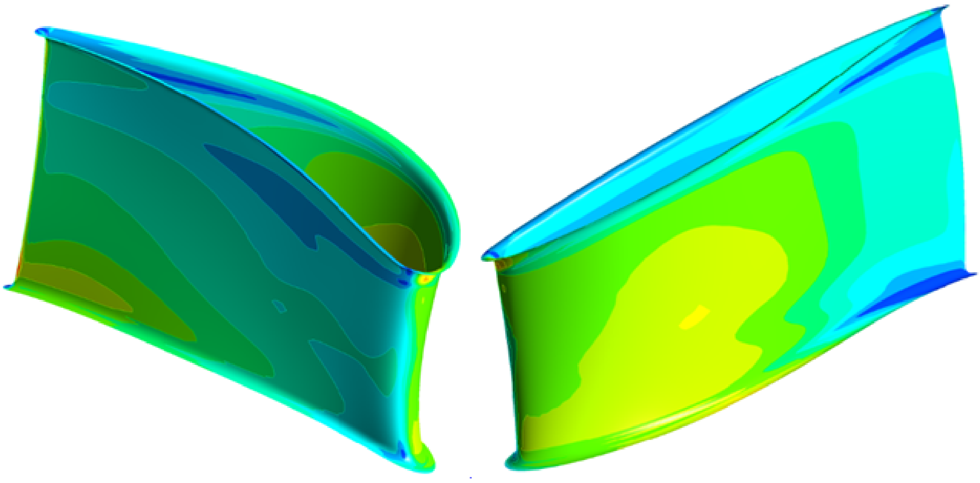

(a) Fully turbulent model.

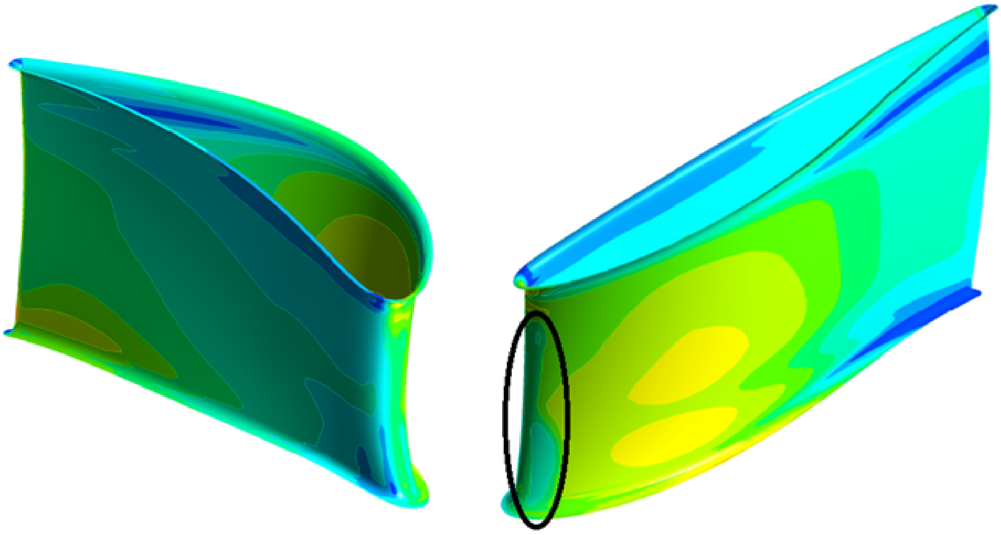

(b) Transitional model.

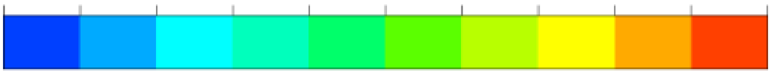

Figure A.1: Wall shear stress.

In A.1, the wall shear stress on the IPV surface is shown for both the fully turbulent SST $k-\omega$ the transitional $\gamma-\theta$ model available in CFX 16.0. These results are for the film cooled steady state case. A small region of low shear stress at the IPV leading edge can be seen. It is circled in black in figure A.1b. This is the laminar region. It is absent in figure A.1a. The remaining surface shows similar levels of wall shear stress. This laminar region is small and should not affect the results too much. Hence, the traditional two equation turbulence model for the unsteady film cooled case was used in order to save time.